

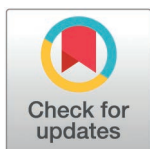
RESEARCH ARTICLE

# The USH3A causative gene *clarin1* functions in Müller glia to maintain retinal photoreceptors

Hannah J. T. Nonarath<sup>1</sup>, Samantha L. Simpson<sup>2</sup>, Tricia L. Slobodianuk<sup>1</sup>, Hai Tran<sup>1</sup>, Ross F. Coltery<sup>2</sup>, Astra Dinculescu<sup>3\*</sup>, Brian A. Link<sup>1\*</sup>

**1** Department Cell Biology, Neurobiology and Anatomy, Medical College of Wisconsin, Milwaukee, Wisconsin, United States of America, **2** Department of Ophthalmology and Vision Sciences, Medical College of Wisconsin, Milwaukee, Wisconsin, United States of America, **3** Department of Ophthalmology, University of Florida, Gainesville, Florida, United States of America

\* [astra@ufl.edu](mailto:astra@ufl.edu) (AD); [blink@mcw.edu](mailto:blink@mcw.edu) (BAL)



## OPEN ACCESS

**Citation:** Nonarath HJT, Simpson SL, Slobodianuk TL, Tran H, Coltery RF, Dinculescu A, et al. (2025) The USH3A causative gene *clarin1* functions in Müller glia to maintain retinal photoreceptors. PLoS Genet 21(3): e1011205. <https://doi.org/10.1371/journal.pgen.1011205>

**Editor:** Cecilia Moens, Fred Hutchinson Cancer Research Center, UNITED STATES OF AMERICA

**Received:** February 29, 2024

**Accepted:** February 4, 2025

**Published:** March 11, 2025

**Copyright:** © 2025 Nonarath et al. This is an open access article distributed under the terms of the [Creative Commons Attribution License](https://creativecommons.org/licenses/by/4.0/), which permits unrestricted use, distribution, and reproduction in any medium, provided the original author and source are credited.

**Data availability statement:** The authors confirm that all data underlying the findings are fully available without restriction. All relevant data are within the paper and its [Supporting Information](#) files.

**Funding:** This work was supported by funding from National Institutes of Health (5R21EY032575 to AD), Foundation Fighting

## Abstract

Mutations in *CLRN1* cause Usher syndrome type IIIA (USH3A), an autosomal recessive disorder characterized by hearing and vision loss, and often accompanied by vestibular dysfunction. The identity of the cell types responsible for the pathology and mechanisms leading to vision loss in USH3A remains elusive. To address this, we employed CRISPR/Cas9 technology to delete a large region in the coding and untranslated (UTR) region of zebrafish *clrn1*. The retinas of *clrn1* mutant larvae exhibited sensitivity to cell stress, along with age-dependent loss of function and degeneration in the photoreceptor layer. Investigation revealed disorganization in the outer retina in *clrn1* mutants, including actin-based structures of the Müller glia and photoreceptor cells. To assess cell-specific contributions to USH3A pathology, we specifically re-expressed *clrn1* in either Müller glia or photoreceptor cells. Müller glia re-expression of *clrn1* prevented the elevated cell death observed in larval *clrn1* mutant zebrafish exposed to high-intensity light. Notably, the degree of phenotypic rescue correlated with the level of *Clrn1* re-expression. Surprisingly, high levels of *Clrn1* expression enhanced cell death in both wild-type and *clrn1* mutant animals. However, rod- or cone-specific *Clrn1* re-expression did not reduce the extent of cell death. Taken together, our findings underscore three crucial insights. First, *clrn1* mutant zebrafish exhibit key pathological features of USH3A; second, *Clrn1* within Müller glia plays a pivotal role in photoreceptor maintenance, with its expression requiring controlled regulation; third, the reliance of photoreceptors on Müller glia suggests a structural support mechanism, possibly through direct interactions between Müller glia and photoreceptors mediated in part by *Clrn1* protein.

## Author summary

Mutations in USH-associated genes profoundly impact patients, affecting auditory, visual, and vestibular function. While the basis of inner ear defects is reasonably well understood for USH and auditory devices can improve hearing, the mechanisms underlying

Blindness (TA-NMT-0621-0811-UFL to AD), E. Matilda Ziegler Foundation for the Blind (to RFC), Foundation Fighting Blindness (PPA-0617-0718 to BAL), National Institutes of Health (R01 EY026559-06A1 to BAL), National Center for Research Resources C06RR016511 (Not applicable). The funders had no role in study design, data collection and analysis, decision to publish, or preparation of the manuscript.

**Competing interests:** The authors have declared that no competing interests exist.

photoreceptor loss are unknown, and there are no approved treatments for vision deficits. In USH3A, the affected gene, *clarin1* (*clrn1*), is predominantly expressed in Müller glia. The role of Müller glia in maintaining photoreceptor health and contributions to USH3 pathology is understudied, in part as *Clrn1* mutant mice - the traditional experimental model used to study retinal diseases - do not phenocopy the photoreceptor loss of USH3 patients. In the present study, we developed a zebrafish model of USH3A that displays many features of the human disease. Our research shows that the loss of *Clrn1* affects actin-based structures of the outer retina, including those of photoreceptor cells and Müller glia. Importantly, we demonstrate that the expression of *Clrn1* in Müller glia, but not rods and cones, alleviated light-induced damage in *clrn1* mutant zebrafish. We also highlight that the dosage of *Clrn1* in Müller glia is critical for maintaining proper photoreceptor function. These findings demonstrate the key contribution of Müller glia to USH pathology and can guide strategies for gene-replacement therapies.

## Introduction

Usher syndrome (USH) is an autosomal recessive disorder characterized by the loss of both hearing and vision. This syndrome accounts for more than half of all hereditary cases of deaf-blindness in the United States [1–4]. USH can be subdivided into three clinical classifications (USH1, USH2, USH3) based on the onset, severity, and progression of hearing loss and vestibular abnormalities. USH is further subtyped depending on the affected gene. For all clinical classifications, hearing loss is the primary identifying symptom. Vision loss presents as retinitis pigmentosa, beginning with the loss of night vision followed by a gradual narrowing of the visual field and blindness.

Although all mouse models of USH display early-onset hearing loss, most fail to present with degenerative retinal phenotypes. This represents a major challenge, hampering the investigation of mechanisms leading to vision loss [5–7]. Potential reasons for the absence of retinal degeneration in murine models include marked interspecies differences in photoreceptor ultrastructure, rod/cone ratio, density and distribution, and a potentially distinct subcellular distribution of some of the USH proteins [8]. Specifically, the mouse retina is rod dominant and the photoreceptors lack well-defined calyceal processes, which have previously been described as being abnormal or absent [8,9]. The calyceal processes are long microvilli-like actin rich structures resembling hair cell stereocilia, that emerge from the apical region of the inner segment (IS) and envelop the base of the outer segment (OS) in rods and cones. This collar-like organization of the calyceal processes is present in zebrafish, frogs, pigs and primates, including humans, but is absent or vestigial in mouse photoreceptors [8,10,11]. Within the human and non-human primate retina, USH1 proteins were reported to localize to the calyceal processes and the inner-outer segment interface [8,12]. The USH1 protein Harmonin was also localized at the tips of the Müller glia apical microvilli and the adherens junctions between Müller glia and photoreceptor cells forming the outer limiting membrane in the human retina [13]. Harmonin localization is consistent with a previous study performed in zebrafish retina [14]. While localization of USH proteins is an important first step in understanding their functions, genetic mutation studies in models capable of replicating the photoreceptor degeneration are critical to understand the underlying mechanisms of USH pathology. Notably, zebrafish loss-of-function models of USH1 and USH2 have been instrumental in characterizing their roles in photoreceptor structure and maintenance [14–18]. In contrast, virtually nothing is known about the mechanisms of retinal degeneration associated with USH3.

Mutations in *CLRN1* gene (clarin1, *USH3A*) encoding a four-transmembrane domain protein (CLRN1), are the leading cause of USH3, resulting in progressive loss of hearing and retinitis pigmentosa in humans, with variable vestibular dysfunction [19–22]. As with other USH-associated proteins, understanding the role of CLRN1 in the retina has been hindered by the lack of a retinal degenerative phenotype in murine models and discrepancies in its reported cellular expression [23]. Specifically, both the *Clrn1* KO and N48K knock-in mouse models of USH3A present with an early-onset hearing loss and profound deafness by postnatal day P30 [7,24]. However, both models lack a retinal degeneration phenotype [7,24]. Our understanding of CLRN1 function primarily comes from cell-culture studies and research of the inner ear in mouse and zebrafish models [7,25–27]. Cell culture experiments have shown that CLRN1 is trafficked to the plasma membrane and may function as a regulator of actin organization [27]. In mouse and zebrafish models of USH3A (*clrn1*), mutant animals presented with disorganized stereocilia, which are apical protrusions composed of actin bundles with mechano-sensory function in auditory and vestibular sensory hair cells [7,28–31]. Previously established USH3A zebrafish mutants presented with hearing deficits and splayed hair cells at larval stages [28]. Mutant animals did not survive into adulthood and there were no obvious changes in retinal morphology and function in larvae [28]. Within the inner ear, the disorganization of hair cell stereocilia prevented the proper transduction of mechanical force from sound, head movement, or gravity into electrical signals. These findings suggest that CLRN1 regulates the formation and maintenance of properly shaped hair bundles in both the outer and inner hair cells of the inner ear [26]. Whether CLRN1 performs a similar role at later stages in maintaining the integrity of actin-rich structures in the retina is unknown.

Published studies indicate *Clrn1* transcripts are abundantly enriched in Müller glia, as compared to other cell types. In the early postnatal mouse retina, mRNA in-situ hybridization analysis revealed that *Clrn1* expression was restricted to the inner nuclear layer (INL) and co-localized with Müller glia cell-specific markers [7,32]. In a cross-species study, in-situ hybridization and single-cell RNAseq analysis revealed that *Clrn1* transcripts in the mouse and human adult retina were concentrated to the INL and explicitly enriched in Müller glia [32]. Other studies based on scRNAseq analysis have also reported that *Clrn1* mRNA is enriched in retinal progenitors and Müller glia across several species, including human, non-human primate, and zebrafish [33–35]. Transcriptomic studies suggest that several other USH1 genes, including *HARMONIN* (USH1C), *CDH23* (USH1D), and *SANS* (USH1G) are also expressed in Müller glia [33]. Additionally, *in vitro* binding studies suggest that CLRN1 and HARMONIN can directly interact [31]. Uncovering the roles of Müller glia-expressed USH proteins in the retina will shed light not only on mechanisms of USH pathology, but also advance our understanding of the relationship between Müller glia and photoreceptors.

## Results

### Development of *clrn1* mutant zebrafish

To develop an USH3A model in zebrafish, 85% of the coding sequence for *clrn1* was deleted through a CRISPR-Cas9 strategy. Specifically, we used one CRISPR gRNA that targeted a region of exon 1 and another CRISPR gRNA designed to target the 3' UTR of *clrn1* (Fig 1). To confirm the deletion and establish a genotyping protocol, primers flanking the cut sites were designed to discriminate the genomic deletion (S1A Fig). Additionally, Sanger sequencing (S1B Fig) and RNAscope for *clrn1* (Fig 1C) were applied to confirm the *clrn1* deletion. Sanger sequencing demonstrated the elimination of the genomic region between the targeted CRISPR cut sites, while RNAscope analysis substantiated the complete loss of *clrn1* transcripts (Fig 1). Furthermore, RNAscope showed that in zebrafish, similar to other species, *clrn1* transcripts

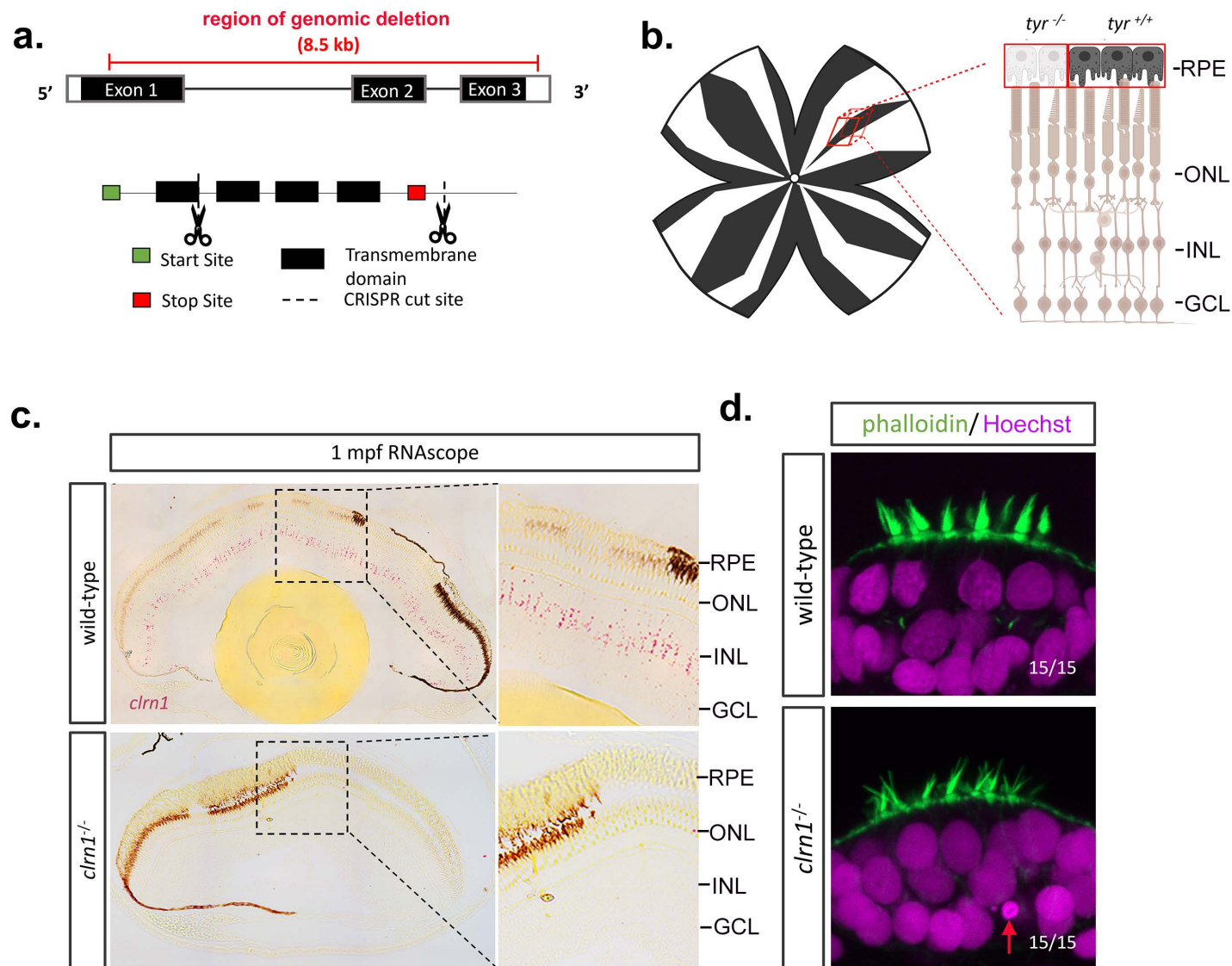


**Fig 1. Development of USH3A zebrafish model.** CRISPR/Cas9 technology was used to generate a large deletion within the *clrn1* gene and establish a germ-line transmitting mutant line. Pairs of CRISPR gRNAs were designed to target Exon 1 and the 3' UTR of *clrn1*. (a) Depiction of CRISPR cut sites in relation to *clrn1* zebrafish exons and protein functional domains. (b) Method to mosaically mutate the tyrosinase gene and deplete pigmentation from the retinal pigment epithelium to allow for RNAscope probe detection. (c) Detection of *clrn1* transcripts (bright red dots) in the inner retina of 1 mpf wild-type zebrafish using the highly sensitive RNAscope in-situ hybridization assay. Retinal Pigment Epithelium (RPE), Outer Nuclear Layer (ONL), Inner Nuclear Layer (INL), and Ganglion Cell Layer (GCL) are labeled in (b) and (c). (d) Phalloidin (actin, green) and Hoechst (nuclei, magenta) staining on 7dpf wild-type and *clrn1*<sup>-/-</sup> larvae to assess inner ear hair cell structure. Red arrow indicates pycnotic nuclei. *n*=15/15 embryos showing normal stereocilia in wild-type and 15/15 embryos showing splayed stereocilia in *clrn1*<sup>-/-</sup> mutants. Schematic in (b) created in BioRender under License: <https://BioRender.com/c00b794>.

<https://doi.org/10.1371/journal.pgen.1011205.g001>

concentrate in the INL of the retina. For this expression analysis, we mosaically deleted tyrosinase using a CRISPR approach so that pigmentation was depleted within some RPE cells (Fig 1B; [36]). We did not detect *clrn1* expression within the RPE. Lastly, to confirm the loss of Clrn1 function, we evaluated previously established hair cell phenotypes of the inner ear associated with USH3 models [7,28]. At 7 dpf, the hair cell organization was grossly altered, with *clrn1*<sup>-/-</sup> zebrafish larvae presenting with splayed stereocilia (Fig 1D). In some animals, pycnotic nuclei were also observed in the hair cells of the anterior macula at the time point investigated (red arrow, Fig 1D). However, in *clrn1*<sup>-/-</sup> larvae no severe vestibular phenotype



was observed, such as the circular swimming pattern reported in the *myo7aa* (USH1B) and *pcdh15a* (USH1F) mutants zebrafish [37–39].

### ***Clrn1*<sup>-/-</sup> adult zebrafish show progressive disruption of the cone photoreceptor mosaic**

Several established zebrafish models of USH do not survive into adulthood, including previously generated *clrn1* mutant zebrafish, preventing the study of disease progression and pathophysiology [28]. However, the *clrn1*<sup>-/-</sup> zebrafish developed for this study do survive into adulthood, providing an opportunity to characterize aged retinal phenotypes. To assess whether mutant retinas show the progressive photoreceptor disorganization and degeneration that is observed in USH3A patients, we utilized optical coherence tomography (OCT), which can provide single cell resolution of cone photoreceptor cell organization. Retinas of wild-type and *clrn1*<sup>-/-</sup> zebrafish were imaged at 4-, 8-, 12-, and 20-months post fertilization (mpf). From the OCT scans, *en face* images of the ultraviolet-sensitive (UV) cone photoreceptor planar organization was assessed by Voronoi cell area, number of neighbors, and intercell distance regularity [40]. Alterations in these measurements are an indication of disrupted cone photoreceptor structure and/or survival [40]. As expected in wild-type zebrafish, a characteristic crystalline lattice of linear columns and rows of UV cone photoreceptors was observed (Fig 2A–2D). At 4 and 8 mpf, *clrn1*<sup>-/-</sup> zebrafish also displayed the highly regular photoreceptor arrangement, although at 8 mpf, there were a few discernable gaps in the mosaic (Fig 2E–2F). By 12 mpf, the *clrn1*<sup>-/-</sup> zebrafish exhibited more areas absent of photoreceptor outer segment reflectance (Fig 2G–2Gi). At 20 mpf, an OCT reflective signal from cone outer segments was unresolvable in 15% of the *clrn1*<sup>-/-</sup> zebrafish (Fig 2H). Among the *clrn1*<sup>-/-</sup> retinas that still exhibited discrete reflective UV cone outer segments, the organization was significantly disrupted, as indicated by the loss of the hexagonal patterning in the Voronoi overlay (Fig 2Hii). In contrast, smaller changes, as part of normal ageing, occurred to the UV cone mosaic of wild-type animals from 4 to 20 mpf (Fig 2A–2D). Collectively, the OCT data suggest age-dependent cone photoreceptor changes due to loss of *Clrn1*.

### **Photopic and scotopic ERG responses are abnormal in *clrn1*<sup>-/-</sup> zebrafish**

To assess whether the loss of *Clrn1* results in retinal dysfunction, we conducted *ex vivo* electroretinography (ERG) on retinas collected from 4- and 12- mpf wild-type or *clrn1*<sup>-/-</sup> zebrafish. Our findings revealed differences in both scotopic and photopic responses at these time points, as illustrated in Fig 3. Notably, we observed considerable variability in the scotopic b-wave among *clrn1*<sup>-/-</sup> fish, with 30% of the *clrn1*<sup>-/-</sup> fish displaying amplitudes greater than those observed in the 4 mpf wild-type zebrafish (S2A Fig). Additionally, significant reductions in the photopic b-wave were observed in 4 mpf *clrn1*<sup>-/-</sup> zebrafish (Fig 3B). Furthermore, differences were noted in the amplitude of the flicker responses at lower frequencies (Figs 3C and S3). These findings suggest defects in visual transduction by at least 4 mpf in *clrn1*<sup>-/-</sup> animals. We were unable to measure ERGs in younger, smaller eyes by our *ex vivo* approach.

Similar distinctions in scotopic and photopic responses were evident in the 12 mpf *clrn1*<sup>-/-</sup> zebrafish when compared to their age-matched wild-type counterparts (Fig 3D–3E). At 12 mpf, the scotopic b-waves were consistently diminished and less variable than the 4 mpf timepoint (Figs 3D and S2C). Furthermore, the significant reduction in the photopic b-wave, coupled with a marked decrease in the photopic flicker response, persisted in the 12 mpf *clrn1*<sup>-/-</sup> zebrafish (Fig 3D and 3F). At 12 mpf, an irregular patterning of the flicker response was also observed at 25 Hz and 30 Hz, suggesting potential deficits in the recovery of cone photoreceptor function between stimulations (S3A Fig).

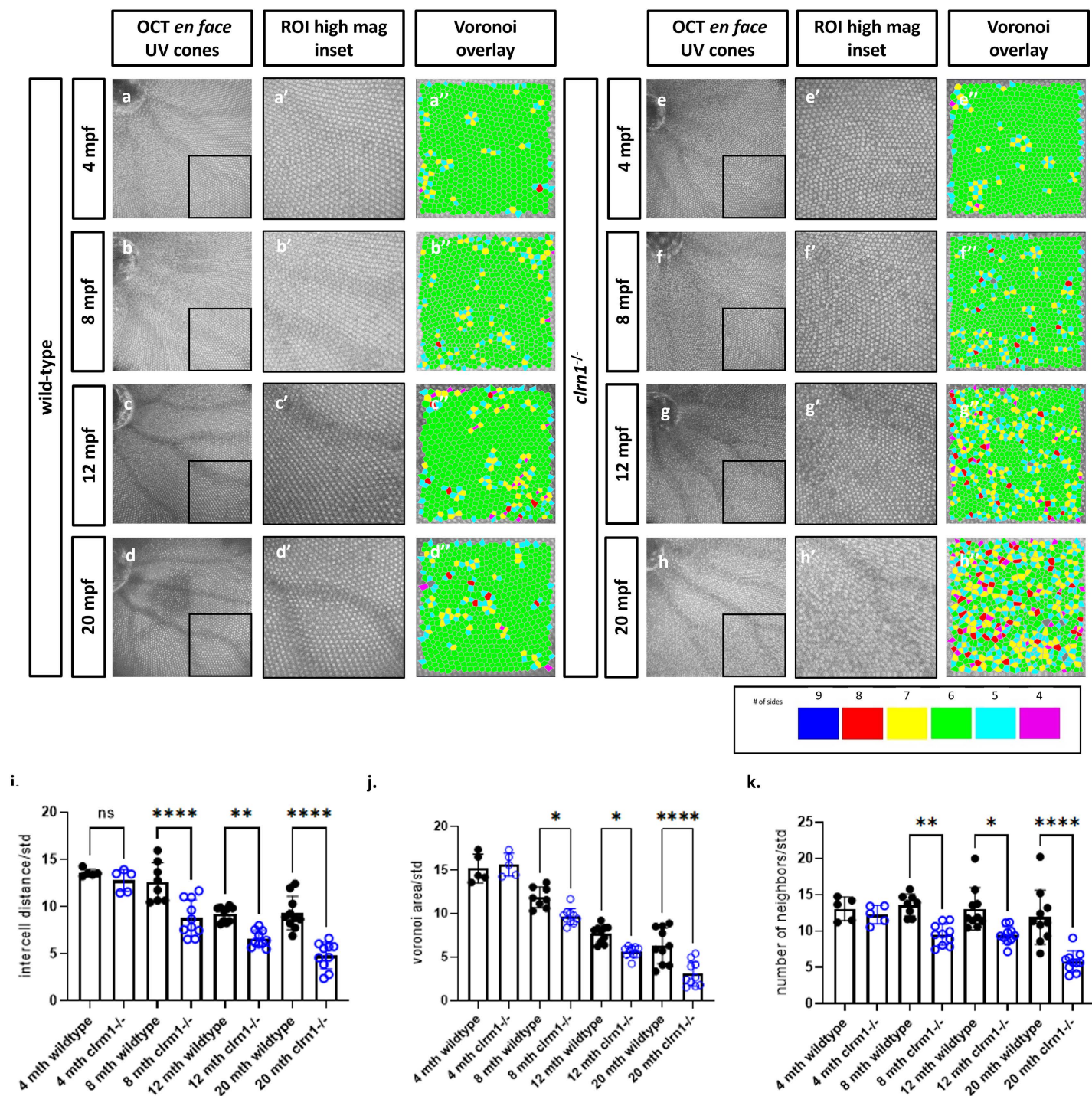


**Fig 2. *clrn1*<sup>-/-</sup> zebrafish present with an altered UV cone mosaic beginning at 8 mpf.** *En face* images of the UV cone mosaic were segmented from OCT scans, a higher magnification ventro-temporal region of interest (ROI) was selected (a'-h') and processed for Voronoi overlay analysis (a''-h'') in wild-type at (a) 4, (b) 8, (c) 12, and (d) 24 mpf, as well as *clrn1*<sup>-/-</sup> zebrafish at (e) 4, (f) 8, (g) 12, and (h) 24 mpf. Quantification of the UV cone mosaic regularity revealed statistically significant differences in (i) intercell distance regularity, (j) number of neighbors regularity and, (k) the Voronoi area regularity at 8 mpf in *clrn1*<sup>-/-</sup> zebrafish compared to wild-type. (\**p*<0.05, \*\**p*<0.01, \*\*\**p*<0.001; Two-way ANOVA).

<https://doi.org/10.1371/journal.pgen.1011205.g002>

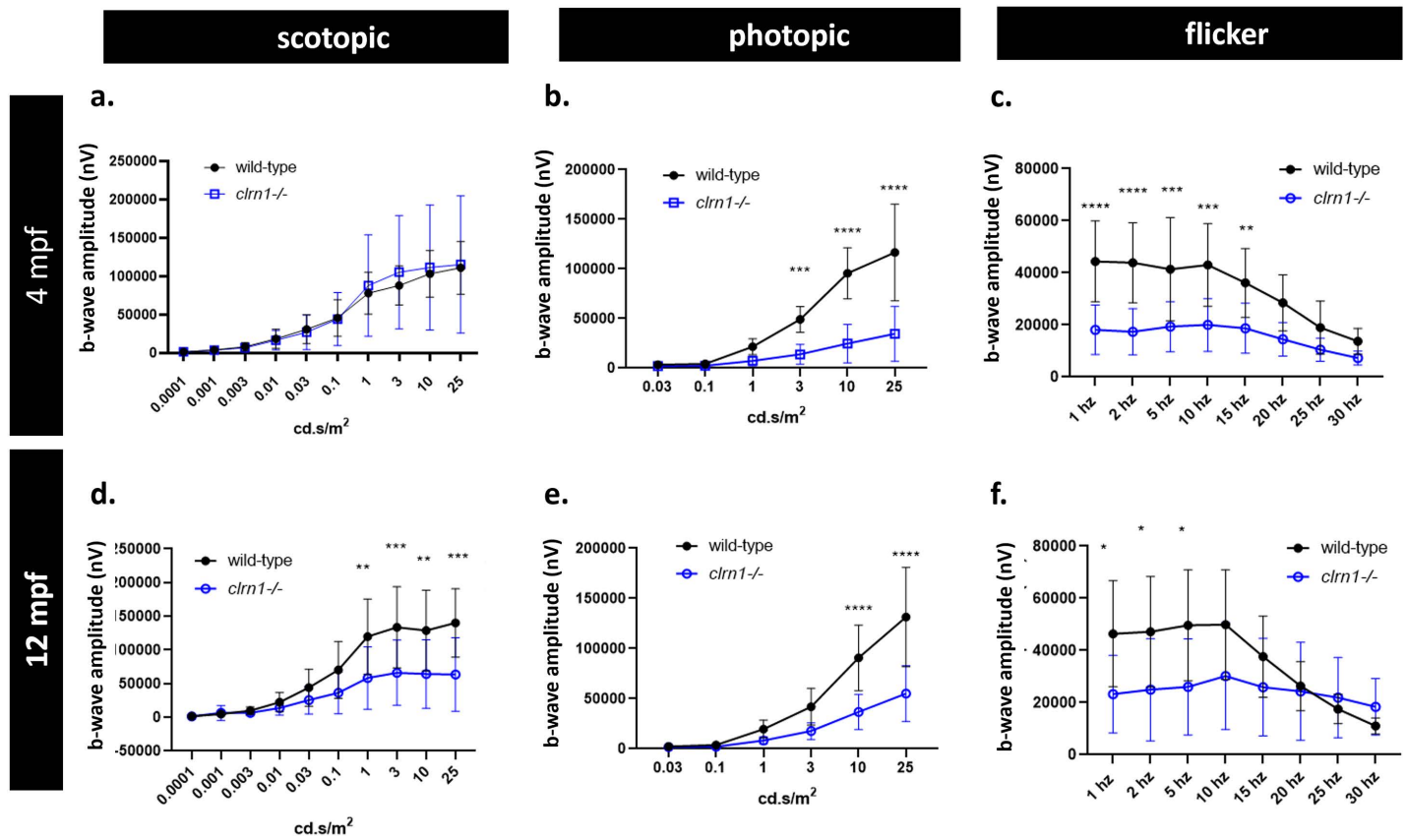


**Fig 3. Scotopic and photopic ERG responses are affected by the loss of *Clrn1*.** Quantification of 4 mpf wild-type and *clrn1*<sup>-/-</sup> ERG b-wave amplitudes for (a) scotopic, (b) photopic, and (c) flicker responses. Quantification of 12 mpf wild-type and *clrn1*<sup>-/-</sup> ERG b-wave amplitudes for (d) scotopic, (e) photopic, and (f) flicker responses. (\**p*<0.01, \*\**p*<0.005, \*\*\**p*<0.001, \*\*\*\**p*<0.0001; One-way ANOVA). Error bars=SD. *n*=10 animals/eyes for each genotype per time-point.

<https://doi.org/10.1371/journal.pgen.1011205.g003>

In addition to amplitude, we evaluated differences in the scotopic and photopic b-wave implicit time. In 4 mpf fish, no significant difference in implicit times between mutants and wild-type siblings was observed (S4A and S4B Fig). At 12 months of age, however, we did observe a significant increase in the photopic b-wave implicit time in *clrn1*<sup>-/-</sup> zebrafish (S4D Fig). Overall, our data suggests that the loss of *Clrn1* affects the function of both rod and cone photoreceptors, or perhaps that of Müller glia which contribute to the ERG b-wave signal.

### Slow and progressive photoreceptor loss in *clrn1*<sup>-/-</sup> zebrafish

Differences in the *clrn1*<sup>-/-</sup> zebrafish photoreceptor mosaic, as detected by OCT, may be attributed to cell death or disruption of the photoreceptor outer segments. Similarly, the differences in the ERG responses observed between *clrn1*<sup>-/-</sup> zebrafish and their wild-type siblings could be due to the loss of photoreceptors or the presence of non-functional photoreceptors. Therefore, we performed histological analysis on retinal sections from 4-, 8-, 12-, and 20-mpf wild-type and *clrn1*<sup>-/-</sup> zebrafish to determine if photoreceptor cells were lost. At 20 mpf, we observed obvious thinning of the ONL in *clrn1*<sup>-/-</sup> zebrafish (Fig 4A), compared to wild-type siblings. We therefore quantified the photoreceptor loss at early stages, and found a slow, but progressive thinning of the ONL starting as early as 4 mpf (Fig 4C). Analysis of rod versus cone nuclei numbers revealed an initial decrease in rod photoreceptors as early as 4 mpf, followed by loss of cones by 8 mpf (Fig 4E-4F). In addition to the decrease in nuclei within the



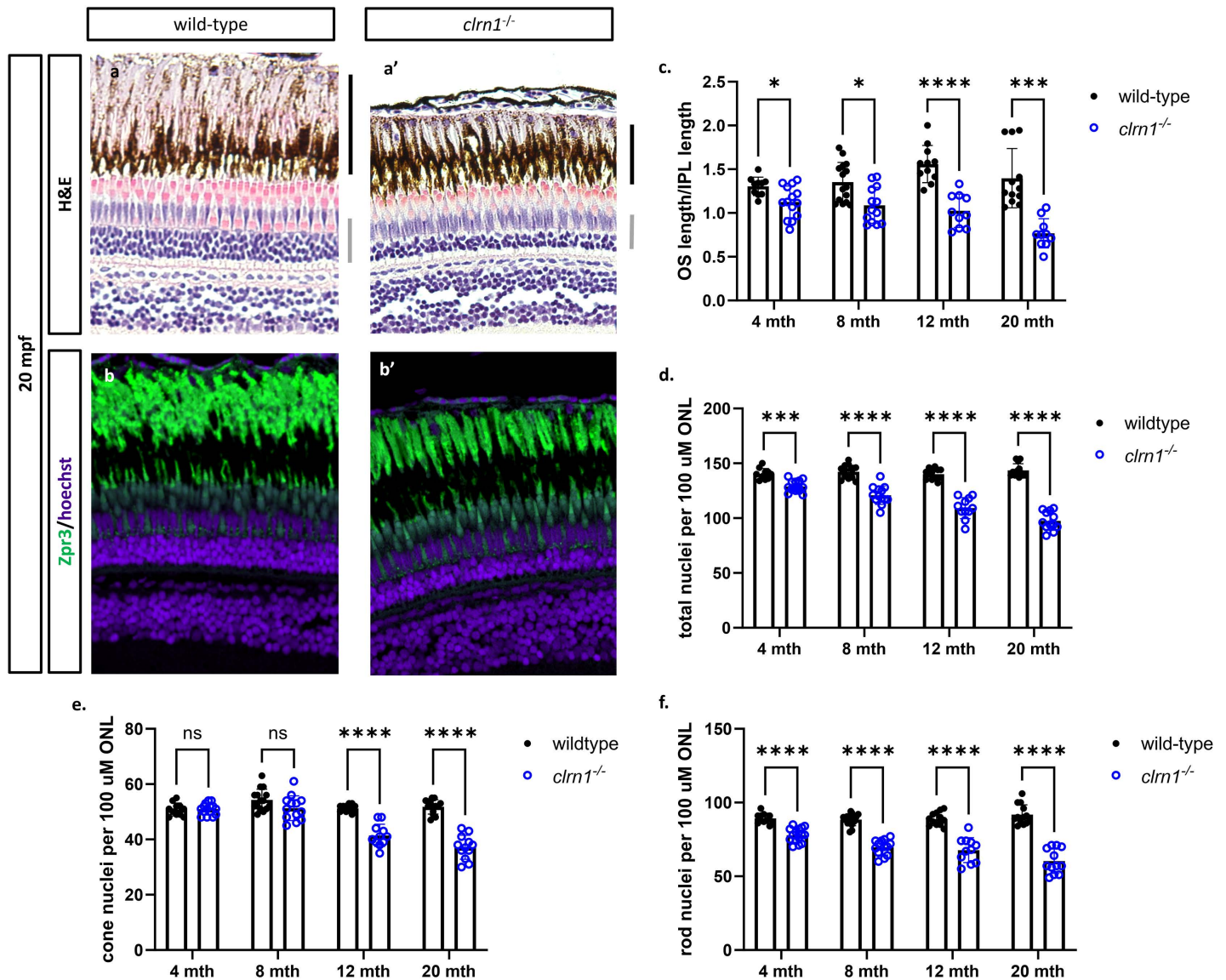


**Fig 4. *clrn1*<sup>-/-</sup> zebrafish present with age-dependent shortening of the rod outer segments and thinning of the outer nuclear layer.** Hematoxylin and eosin-stained paraffin section from (a) 20 mpf wild-type and (a') *clrn1*<sup>-/-</sup> zebrafish. Staining for Zpr3+ (Rhodopsin and green opsin), primarily marking rod photoreceptor outer segments (green) on paraffin sections from (b) 20 mpf wild-type and (b') *clrn1*<sup>-/-</sup> zebrafish. (c) Quantification of rod outer segments (OS) length at 4, 8, 12, and 20 mpf. (d) Quantification of total photoreceptors per 100  $\mu$ m of ONL length at 4, 8, 12, and 20 mpf. Analysis of (e) rod and (f) cone photoreceptors in wild-type and *clrn1*<sup>-/-</sup> zebrafish at 4, 8, 12, and 20 mpf. (a-b') The black bars in (a') denote the location of the rod OS, and the grey bar notes the outer nuclear layer. (ns, not significant =  $p > 0.05$ , \* $p < 0.05$ , \*\* $p < 0.01$ , \*\*\* $p < 0.005$ , \*\*\*\* $p < 0.001$ ; One-way ANOVA). (n=12-15 for each genotype per time-point).

<https://doi.org/10.1371/journal.pgen.1011205.g004>

ONL, there was also a shortening of the rod outer segments, a phenotype frequently observed in models of retinal degeneration [41–43] (Fig 4B and 4C).

Zebrafish can regenerate a damaged retina, although not all photoreceptor degenerations trigger this response [44]. To assess potential cell regeneration we evaluated BrdU incorporation, which is often used to mark regeneration. We detected a small, but significant increase in BrdU-positive cells at 4 mpf (S5 Fig). At subsequent ages, BrdU incorporation remained moderately elevated (S5E and S5F Fig), despite the overall loss of *clrn1*<sup>-/-</sup> photoreceptor cells with age. The observed BrdU-positive cells may represent attempted but inadequate regeneration, and/or dying photoreceptor cells undergoing DNA repair; which has been reported [45–50].



## Enhanced photoreceptor cell death to constant, high-intensity light in *clrn1*<sup>-/-</sup> zebrafish

Previous studies have shown that photoreceptor survival in mutant USH1 and USH2 larvae was compromised in a high-intensity light stress assay, which causes oxidative damage, endoplasmic reticulum stress, and alterations to autophagy [16,17,51]. To determine if similar sensitivities occurred in our USH3A zebrafish model, animals were exposed to constant, high-intensity light to enhance cell stress from 5–7 dpf (Fig 5A). Under standard lighting conditions, we did not observe histological changes or significant differences in cell death markers in either wild-type or *clrn1* mutant larvae (Fig 5B–5D). Similarly, in the wild-type fish exposed to constant, high-intensity light, we did not observe any histological changes or induction of cell death. Conversely, *clrn1*<sup>-/-</sup> fish exposed to constant, high-intensity light presented with a significant increase in the number of pyknotic nuclei in the ONL layer, indicating cell death (Fig 5B, 5C and 5E). In addition to the presence of pyknotic nuclei, there was a significant increase in TUNEL-positive nuclei in the ONL, indicative of apoptosis (Fig 5B and 5D). We did not observe an increase in the abundance of pyknotic nuclei or TUNEL-positive cells in the other retinal layers of *clrn1*<sup>-/-</sup> fish.

As evident by ERG results, both rods and cones were affected by the loss of *Clrn1*. To discern if cell death in the ONL, following light stress, occurred in rods and/or cones, we stained with fluorescent wheat germ agglutinin (WGA) and peanut agglutinin (PNA), to label the rod and cone outer segments, respectively. In light-stressed *clrn1*<sup>-/-</sup> zebrafish, there was a significant decrease in WGA and PNA-positive outer segments in the peripheral and central retina of *clrn1*<sup>-/-</sup> zebrafish, compared to that of wild-type siblings (Fig 5F–5I). We also noted a small, but significant decrease in the number of rod and cone outer segments in the peripheral retina, but not the central retina of *clrn1*<sup>-/-</sup> 7 dpf larvae under control lighting conditions (Fig 5E–5I). Collectively, data indicates that at the time point investigated, the rod and cone photoreceptors in *clrn1*<sup>-/-</sup> zebrafish show signs of dysfunction and are sensitized to the cellular stresses induced by elevated light exposure.

Along with investigating cell death, we also evaluated potential functional changes following light damage. Using an optomotor response (OMR) assay, we tested larvae on their ability to detect direction changes. Unexpectedly, we observed functional deficits in the *clrn1*<sup>-/-</sup> zebrafish housed under standard husbandry conditions compared to wild-type animals (S6 Fig). The failure of mutant larvae to respond to OMR stimulus under control lighting conditions suggests baseline visual impairment.

## Loss of *Clrn1* disrupts actin-rich structures of the outer retina

Thus far, data highlight that the loss of *Clrn1* in zebrafish results in progressive photoreceptor dysfunction and degeneration along with sensitization to light-mediated stress. Therefore, we focused on identifying retinal changes associated with the loss of *Clrn1*. Previous cell culture experiments and *in vivo* studies of inner ear hair cells suggest a possible role of *CLRN1* in the regulation of the F-actin cytoskeleton [27,29–31]. To explore the function of *Clrn1* in the retina, we assessed for potential changes in actin-based structures of the outer retina including the adherens junctions of the OLM, calyceal processes of photoreceptors, and apical microvilli of Müller glia. We first used a *gfap*:GFP transgenic line which expressed cytoplasmic GFP specifically within Müller glia and highlights cell morphology. At 7 dpf and at low magnification, no obvious defects were noted in mutant Müller glia (Fig 6A). Higher magnification, however, suggested that the apical microvilli of Müller glia were reduced in number and disorganized – reminiscent of the splayed stereocilia phenotype of the inner ear hair cells (Fig 6B). Quantification of the number and length of Müller glia apical projections confirmed these impressions (Fig 6C and 6D).

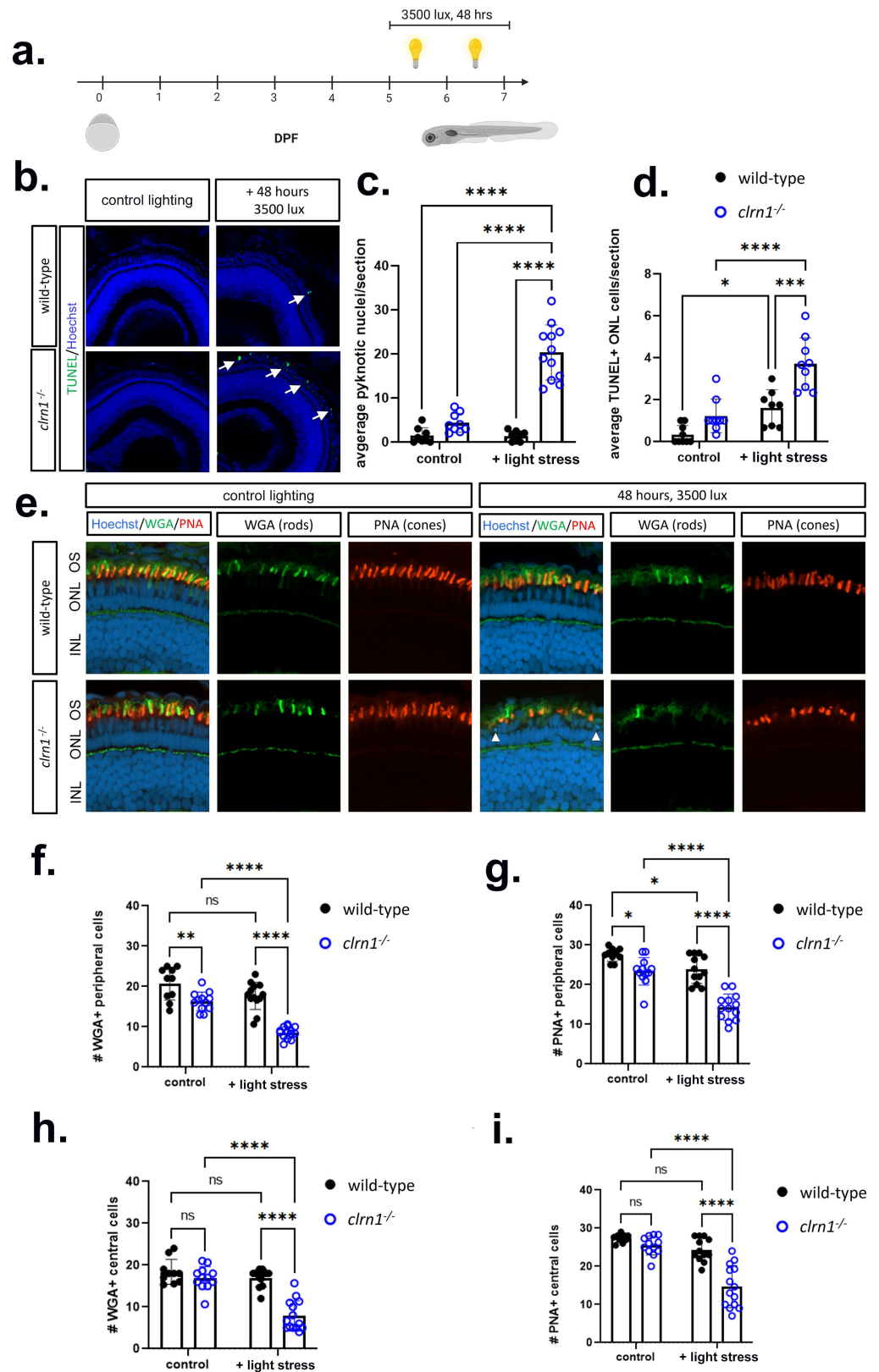


**Fig 5. High-intensity light induces rod and cone cell death in *clrn1*<sup>-/-</sup> zebrafish.** (a) Overview of light stress assay: larvae were treated with 3500 lux for 48 hours from 5–7 dpf. (b) Representative images of TUNEL-positive

photoreceptors (white arrows) on cryosectioned retina from 7 dpf wild-type (upper panels) and *clarin1*<sup>-/-</sup> (lower panels) zebrafish revealed a significant increase in the (c) average number of pyknotic nuclei and (d) TUNEL-positive cells per section in the ONL of *clarin1*<sup>-/-</sup> zebrafish. (e) Retinal sections from 7dpf control or light-stressed wild-type (upper panels) and *clarin1*<sup>-/-</sup> zebrafish (lower panels) stained with wheat germ agglutinin (WGA, rods, green) and peanut agglutinin (PNA, cones, red) as well as Hoechst to label nuclei (white arrow heads denote pyknotic cells). Quantification of (f) WGA- and (g) PNA-positive outer segments along a 100  $\mu$ m region of the peripheral retina revealed a significant decrease in rod and cone outer segments in control *clarin1*<sup>-/-</sup> zebrafish, which was exacerbated under light stress. Quantification of (h) WGA- and (i) PNA-positive outer segments along a 100  $\mu$ m section of the central retina revealed a significant decrease in rod and cone outer segments in light-damaged *clarin1*<sup>-/-</sup> zebrafish. (\* $p$ <0.05, \*\* $p$ <0.01, \*\*\* $p$ <0.001; Two-way ANOVA). Error bars=SD. Scale Bar = 100  $\mu$ m. n=10-15 per genotype for each condition. OS, Outer Segment; ONL, Outer Nuclear Layer; INL, Inner Nuclear Layer. Schematic in (a) created in BioRender under License: <https://BioRender.com/k07v149>.

<https://doi.org/10.1371/journal.pgen.1011205.g005>

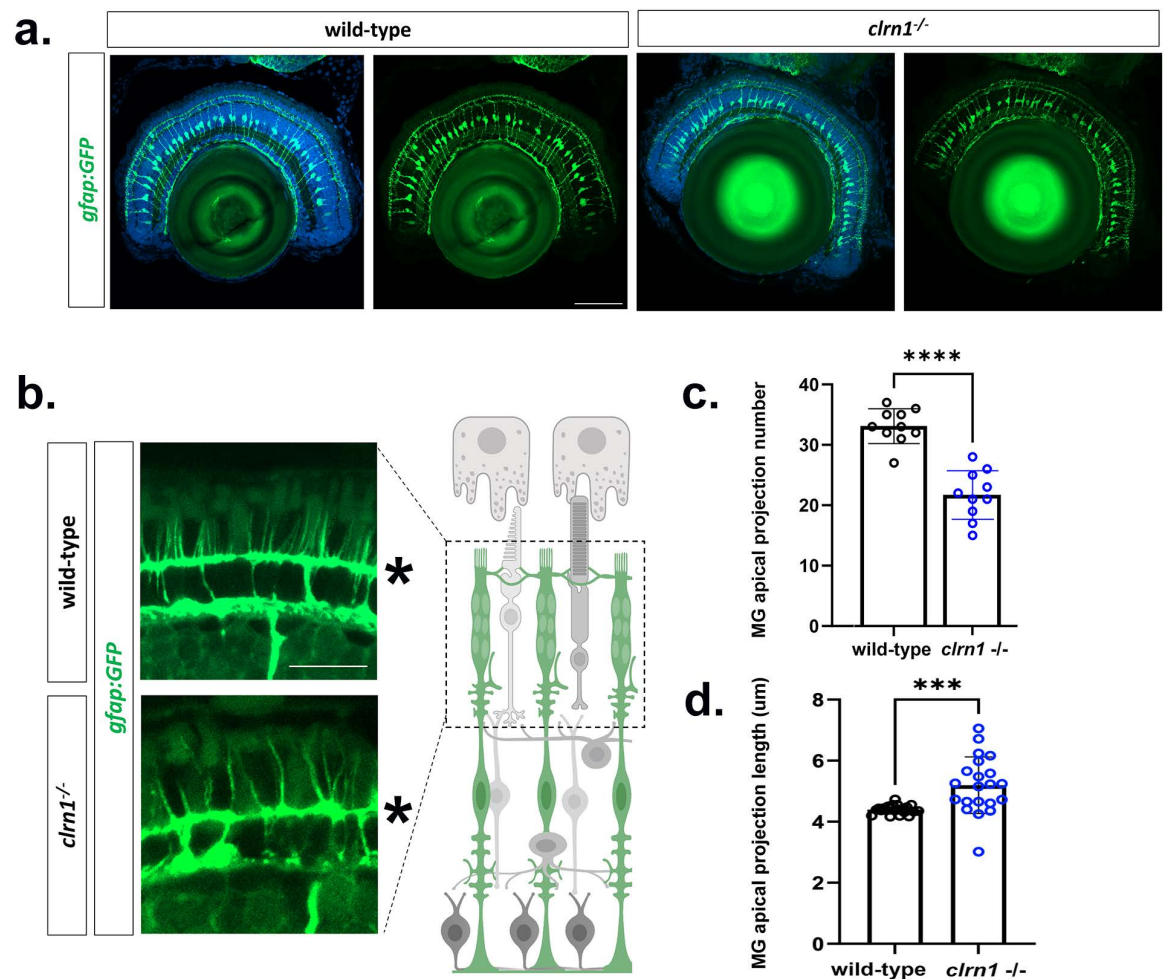


**Fig 6. Actin is disorganized in the outer retina of *clarin1*<sup>-/-</sup> mutant zebrafish.** Transverse sections from 7 dpf wild-type and *clarin1*<sup>-/-</sup> Tg(*gfp:gfp*) zebrafish (a) showing the ordered spacing and radial expansion of Müller glia of both wild-type and *clarin1* mutant retina. (b) Higher magnification images of Müller glia apical projections of wild-type and *clarin1*<sup>-/-</sup> zebrafish highlights disorganization of the mutant apical microvilli (c). Quantification of total Müller glia (MG) apical microvilli within a 40  $\mu$ m<sup>2</sup> region of the central retina of wildtype and *clarin1*<sup>-/-</sup> zebrafish (d). Müller glia (MG) apical microvilli length beyond the OLM (labeled with asterisk in b.) for wild-type and *clarin1*<sup>-/-</sup> 7 dpf zebrafish. (\*\*\* $p$ <0.005, \*\*\*\* $p$ <0.001; Students T-test). Scale bars = (a) 100  $\mu$ m; (b) 50  $\mu$ m. Data points in (c,d) represent measurements from n = 10 zebrafish each condition. For (d) data points are an average per zebrafish in which 9-22 projections quantified. Schematic in (b) created in BioRender under License: <https://BioRender.com/x12n534>.

<https://doi.org/10.1371/journal.pgen.1011205.g006>



A common phenotype of several USH1 zebrafish mutants is disrupted photoreceptor calyceal processes [15,51]. To investigate the cone calyceal processes of *clrn1*<sup>-/-</sup> mutants, we developed a transgenic line, *Tg(gnat2:Lifect-mCherry)*, that expresses Lifect, an F-actin binding protein [52,53], under the cone-specific *gnat2* promoter. Co-labeling of Lifect-mCherry with an antibody against Espin, an actin cross-linking protein and marker of calyceal processes (Sharkova 2024-PMID: 38477343), showed that the concentrated signal of cone-expressed Lifect-mCherry highlights the calyceal processes (S7 Fig). Transverse cryosections showed enriched staining of Lifect-mCherry within the calyceal processes, and to a lesser extent at the adherens-type junctions of the OLM (Fig 7A). Calyceal processes of *clrn1*<sup>-/-</sup> mutants were disorganized and showed a spectrum of phenotypes. The majority of mutant retinas showed elongated, moderately splayed calyceal processes that were reduced in number compared to those of wild-type siblings (Fig 7B). Others were more severely splayed and contained Lifect-mCherry puncta (Fig 7C). Lifect-mCherry puncta were also noted at the OLM (Fig 7Cii). Given the similarity of phenotypes between mutant Müller glia apical microvilli and the photoreceptor calyceal processes, we combined the *gnat2:Lifect-mCherry* and *gfap:GFP* transgenes to investigate potential associations between these actin-rich structures. We found that in wild-type retina the apical projections of Müller glia were in close association with cone calyceal processes (Fig 7A). However, this association was often disrupted in *clrn1*<sup>-/-</sup> retina (Fig 7B and 7C).

*En face* imaging of *Tg(gfap:GFP; Tg(gnat2:Lifect-mCherry))* transgenic zebrafish at the level of UV cone photoreceptor outer segments confirmed the association of the Müller

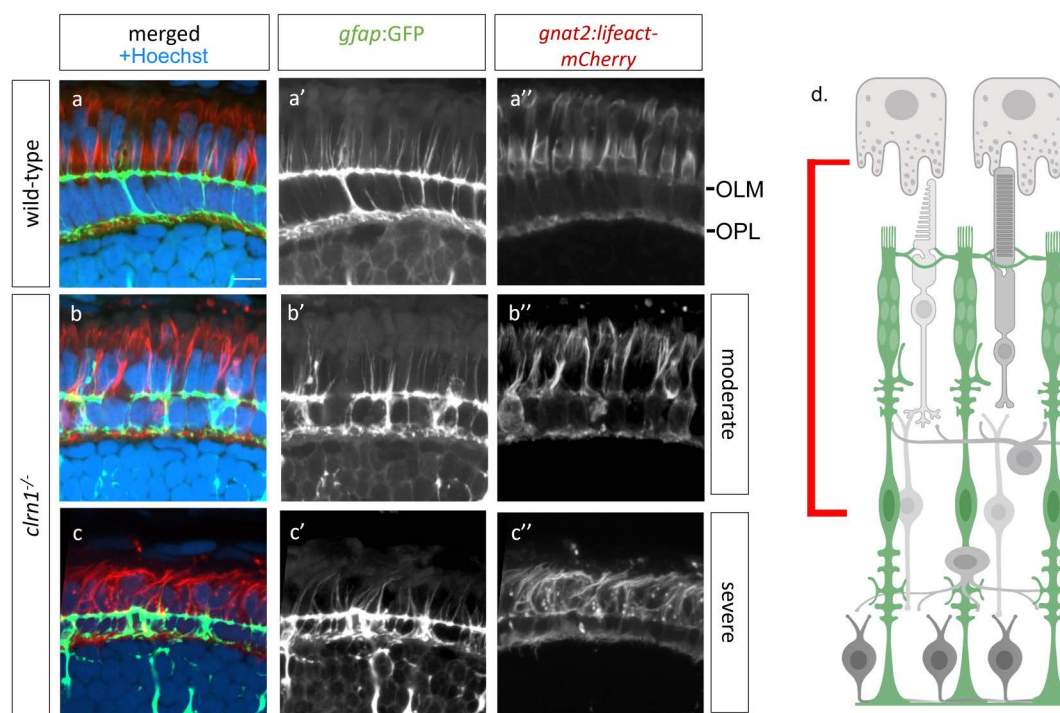


**Fig 7. Apical processes of Müller glia and calyceal processes of cone photoreceptors are disorganized in *clrn1*<sup>-/-</sup> retina.** Transverse sections from 7 dpf (a) wild-type and (b,c) *clrn1*<sup>-/-</sup> mutant zebrafish each expressing the *Tg(gfap:GFP)*; *Tg(gnat2:Lifect-mCherry)* transgenes highlighting either (b) moderately or (c) more severely altered Müller glia apical microvilli projections (b',c') and cone-specific actin structures (b'', c'') in *clrn1*<sup>-/-</sup> mutants. (d) Cartoon showing the area imaged (red bar). Scale bar = 10  $\mu$ m. OLM, Outer limiting membrane; OPL, Outer plexiform layer. Schematic in (d) created in BioRender under License: <https://BioRender.com/x12n534>.

<https://doi.org/10.1371/journal.pgen.1011205.g007>

glia apical projections with cone calyceal processes (Fig 8A-8H). The calyceal processes present as mCherry-positive rings with embedded puncta, highlighting bundled calyceal actin (Fig 8B). In close proximity to each actin ring, we found GFP puncta, corresponding to the Müller glia apical microvilli (Fig 8C and 8D). Within each actin ring, there are on average 5-6 associated Müller glia projections. In *clrn1*<sup>-/-</sup> zebrafish, we observed regions of disrupted actin ring formation (Fig 8F-8H). The Müller glia apical projections are also more irregular in their shape and pattern and have reduced association with the cone actin structures (Fig 8E and 8H). *En face* image comparison of wild-type and *clrn1*<sup>-/-</sup> retina at the level of the OLM confirmed altered cone photoreceptor actin and Müller glia association (Fig 8I-8N). Specifically, we observed regions of actin accumulation, which was not evident in wild-type animals (Fig 8I and 8M). Analysis of the Müller glia morphology also showed changes in the projections that envelop the photoreceptors at the OLM (Fig 8I and 8L).

At the cellular-molecular level, these data suggest alteration to the adherens junctions within the OLM of *clrn1*<sup>-/-</sup> mutants. Because of these changes, we immunostained for N-cadherin, a component of the OLM junctions. In a previous *in vitro* study using overexpressed HA-tagged CLRN1, immunoprecipitation assays with an anti-HA antibody followed by proteomic

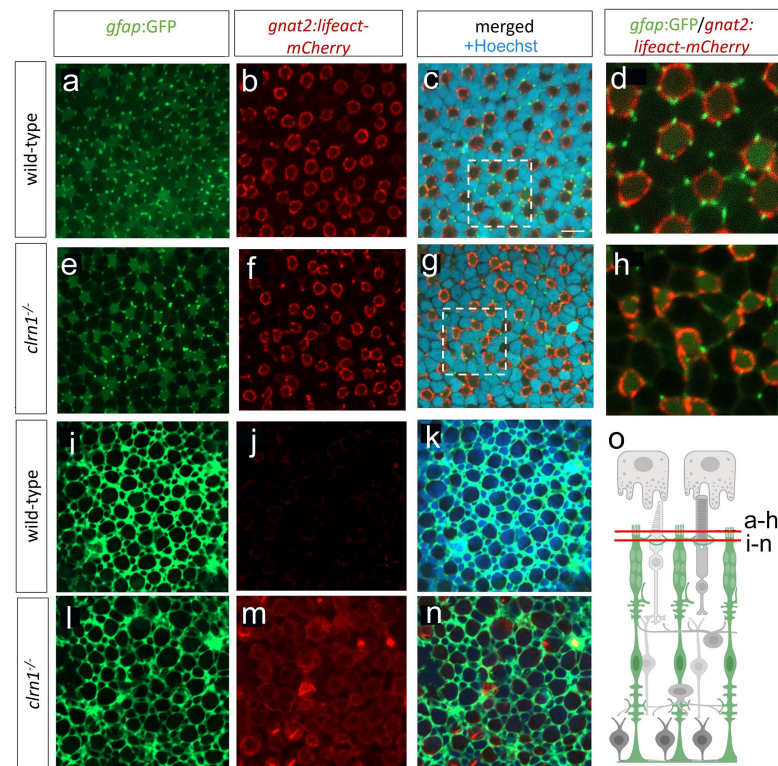


**Fig 8. Interactions between Müller glia and cone photoreceptor cells are disorganized in *clrn1*<sup>-/-</sup> zebrafish.** *En face* images from Tg(*gfap*:GFP); Tg(*gnat2*:Lifeact-mCherry) 7 dpf transgenic zebrafish at the level of UV cone outer segments in either (a-d) wild-type or (e-h) *clrn1*<sup>-/-</sup> retina. Comparison of higher magnification images of (d) wild-type versus (h) *clrn1*<sup>-/-</sup> highlight abnormal interactions between Müller glia apical processes and cone calyceal processes within mutants. (i-n) *En face* images from Tg(*gfap*:GFP); Tg(*gnat2*:Lifeact-mCherry) 7 dpf transgenic zebrafish at the level of the OLM just apical of the adherens junctions, Müller glia processes encircle photoreceptors. Comparison of (i) wild-type versus (l) *clrn1*<sup>-/-</sup> highlight disorganization in mutants. At this image plane, actin is not well detected in (j) wild-types, but accumulates in (m) *clrn1*<sup>-/-</sup> cone photoreceptors. (o) Cartoon showing the imaged planes. Scale bar (c) = 5  $\mu$ m. Schematic in (o) created in BioRender under License: <https://BioRender.com/x12n534>.

<https://doi.org/10.1371/journal.pgen.1011205.g008>

analysis identified N-cadherin as one potential CLRN1 binding partner [27]. In wild-type animals, as anticipated, we observed an even distribution of N-cadherin staining along the junctions of the OLM. This was observed in transverse sections of the retina (Fig 9A and 9Ai), as well as in z-projections of confocal images rotated 90° to show the OLM from a planar, *en face* view (Fig 9Ai). In *clrn1*<sup>-/-</sup> zebrafish, N-cadherin staining appeared less evenly distributed at this region (Fig 9B and 9Bi). Quantitation of fluorescence intensity supports this impression (Fig 9D). From the *en face* view, N-cadherin immunofluorescence formed rings, that appeared disorganized in *clrn1*<sup>-/-</sup> mutants (Fig 9Bi). Quantitation of N-cadherin ring diameter did not show a statistically significant difference ( $p=0.15$ ), although there was a trend towards larger diameters in the *clrn1*<sup>-/-</sup> mutant OLM (Fig 9E). In addition, N-cadherin staining at the OLM appeared expanded and disorganized (Fig 9B). This phenotype is likely due to *clrn1*<sup>-/-</sup> mutants being sensitized to the methanol treatment performed with N-cadherin staining, as histology and other marker analyses which do not require methanol treatment did not show this degree of OLM expansion. Ultra-structural analysis of the OLM junctions revealed that the loss of N-cadherin staining was not due to the failure of junction formation in the absence of Clrn1 (S8 Fig). Outside of the OLM, N-cadherin staining was occasionally mis-localized in a radial pattern extending basally within the mutant retina, perhaps representing mislocalized N-cadherin within Müller glia (labeled by asterisks, Fig 9B). Overall, analysis of actin staining, Müller glia morphology, and N-cadherin staining at the OLM suggests differences in the structural integrity of the OLM in *clrn1*<sup>-/-</sup> mutants.

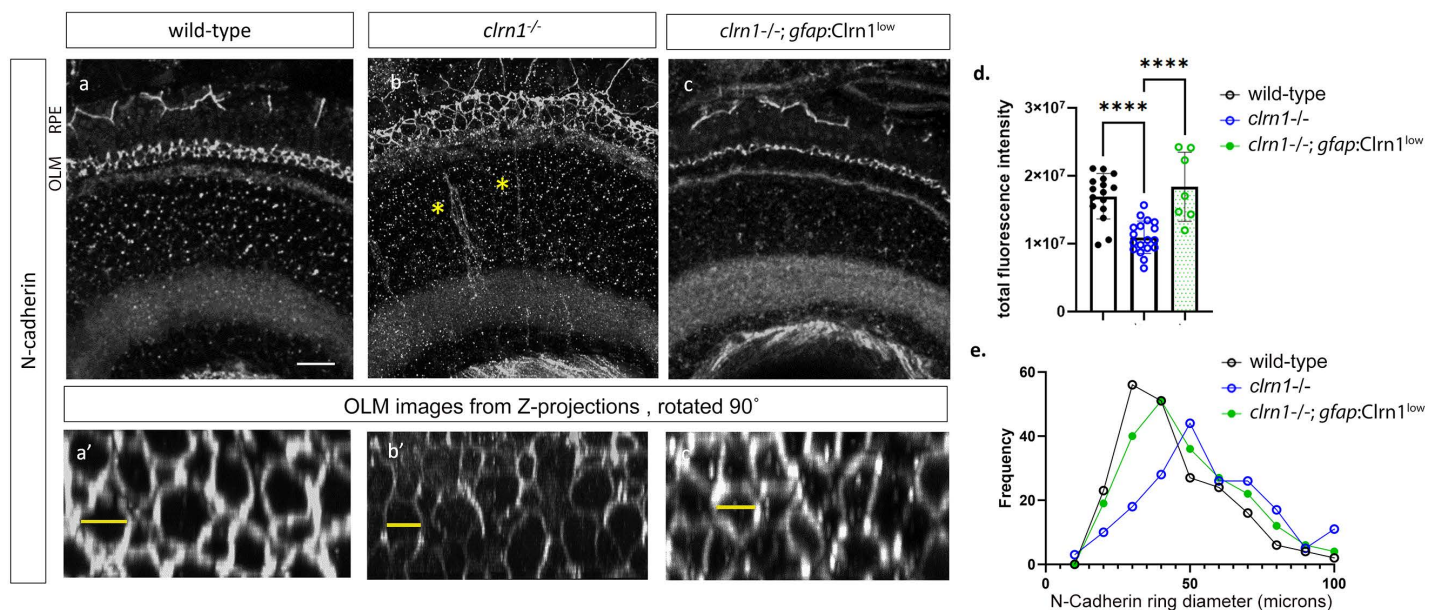


**Fig 9. Expression of N-cadherin is reduced in *clrn1*<sup>-/-</sup> zebrafish.** Confocal microscope images of N-cadherin immunostaining in transverse cryosections of retinas from 7 dpf (a) wild-type, (b) *clrn1*<sup>-/-</sup>, and (c) *clrn1*<sup>-/-</sup>; *Tg(gfap:Clrn1*<sup>low</sup>). Images of N-cadherin staining in the OLM (a', b', c') were generated by rotating projected Z-stacks 90° at the level of the OLM. The OLM and RPE are denoted to the left of panel (a). Yellow asterisks in (b) indicate delocalized N-cadherin within the inner nuclear layer. (d) Quantitation of N-cadherin fluorescence intensity from 300  $\mu\text{m}^2$  central retinal regions revealed that N-cadherin staining was reduced in *clrn1*<sup>-/-</sup> but not in *clrn1*<sup>-/-</sup>; *gfap:Clrn1*<sup>low</sup> ( $n=12$  eyes each genotype). (e) N-Cadherin ring diameter frequency distribution for each genotype. Example measurements marked by yellow lines. Data points in (e) represent 35 rings scored in 300  $\mu\text{m}^2$  central retina region ( $n = 12$  eyes each genotype). (\*\*\*\* $p<0.001$ ; One-way ANOVA). Error bars=SD. Scale Bar=10  $\mu\text{m}$ .

<https://doi.org/10.1371/journal.pgen.1011205.g009>



## Re-expression of *Clrn1* in the Müller glia corrects Müller glia projections and N-cadherin localization

Because of prominent *Clrn1* expression in Müller glia, we explored whether re-expression of *Clrn1* only within Müller glia could rescue the retinal defects caused by its global loss. Specifically, we developed two *Tg(gfap:Clrn1-2A-GFP)* lines (S9A Fig). The 2A peptide sequence induces ribosomal skipping during translation resulting in two proteins from a single transcript, facilitating the identification of cells expressing *Clrn1* without hindering *Clrn1* function by the addition of an N- or C-terminus epitope [54]. Additionally, because *clrn1* and *gfap* are co-transcribed, the measure of GFP fluorescence intensity allows for relative quantification of transgene abundance and, therefore, an indirect estimate of *Clrn1* re-expression levels. During the development of the F1 generation, two lines, designated as high re-expression (*gfap:Clrn1<sup>high</sup>*) and low re-expression (*gfap:Clrn1<sup>low</sup>*) were identified that differed significantly in their level of GFP fluorescence (S9B Fig). Differences in the expression levels between the *gfap:Clrn1<sup>low</sup>* and *gfap:Clrn1<sup>high</sup>* were quantified on the F2 generation by measuring the total GFP fluorescence intensity (S9C Fig). The number of GFP-positive offspring from the F2 generation was also tracked to confirm germline transmission from a single genomic locus for each line.

We first assessed Müller glia structure in wild-type and *clrn1<sup>-/-</sup>* zebrafish expressing the *gfap:Clrn1<sup>low</sup>* or *gfap:Clrn1<sup>high</sup>* transgenes. Because the GFP signal from the *gfap:Clrn1<sup>low</sup>* line was quenched during the process of fixation to levels beyond detection by confocal microscopy, the line was crossed onto a *Tg(gfap:GFP)* background thus enabling evaluation of Müller glia structure. Analysis of Müller glia structure in the *gfap:Clrn1<sup>high</sup>* transgenic zebrafish, in either wild-type or *clrn1<sup>-/-</sup>* mutants, revealed alterations to not only Müller glia but also photoreceptor cells. Specifically, Müller glial processes associated with photoreceptor synapses and the OLM were disorganized (S10 Fig). In addition, the apical microvilli were reduced – even beyond that of *clrn1<sup>-/-</sup>* mutants alone. Within photoreceptors, actin staining (phalloidin) within the region of the outer segments appeared enhanced and disorganized, likely reflecting the overall structural disruption of photoreceptor outer segments. In *clrn1<sup>-/-</sup>* zebrafish expressing the *gfap:Clrn1<sup>low</sup>* transgene, the Müller glia synaptic and OLM projections, as well as the apical microvilli, showed wild-type morphology (S10A–S10C Fig). Similarly, within photoreceptors, defective phalloidin staining was partially rescued. We also observed an increase in the localization of N-cadherin along the junctions of the OLM and an improvement in the distribution of N-cadherin along these junctions within *clrn1<sup>-/-</sup>* *Tg(gfap:Clrn1<sup>low</sup>)* zebrafish (Fig 9C–9E). This analysis overall indicates the importance of appropriate levels of *Clrn1* within Müller glia for the structural integrity of the outer retina.

## Targeted re-expression of *clrn1* in Müller glia ameliorates light damage-induced cell death

To determine whether targeted re-expression of *clrn1* in Müller glia could serve as a therapeutic option for preventing or slowing retinal degeneration in USH3A, we subjected *gfap:Clrn1* transgenic zebrafish to high-intensity light treatment, which was previously established to induce cell death in *clrn1<sup>-/-</sup>* zebrafish (Fig 5). For this experiment, we treated wild-type and *clrn1<sup>-/-</sup>* zebrafish carrying the *gfap:GFP* control transgene and the high and low *Clrn1* re-expression transgenes. As before, larvae were exposed to either standard or high-intensity light from 5 to 7 dpf. Several important observations were made from these studies. First, low *Clrn1* re-expression within Müller glia of *clrn1<sup>-/-</sup>* mutants rescued photoreceptor cell death from light stress, as measured by pyknotic nuclei or TUNEL labeling. Low *Clrn1* expression in wild-type did not affect wild-type retina. However, high *Clrn1* re-expression within Müller

glia was damaging to photoreceptors in either normal or light stressed conditions, and in either wild-type or *clrn1*<sup>-/-</sup> mutants (Fig 10). These results both highlight the potential for gene therapy and emphasize the importance of Clrn1 dosage.

Due to conflicting reports on whether Clrn1 is expressed in the photoreceptor layer [7,25,32–35], we undertook a similar approach to re-express Clrn1 in the rod and cone photoreceptors. We established lines for rod-specific (*Tg(rho:Clrn1-2A-mCherry)*) and cone-specific (*Tg(gnat2:Clrn1-2A-mCherry)*) Clrn1 expression. However, we were unable to isolate multiple lines of each with different levels of expression. We also established the respective control lines, *Tg(rho:mCherry)*, *Tg(gnat2:GFP)*. Light stress experiments were conducted

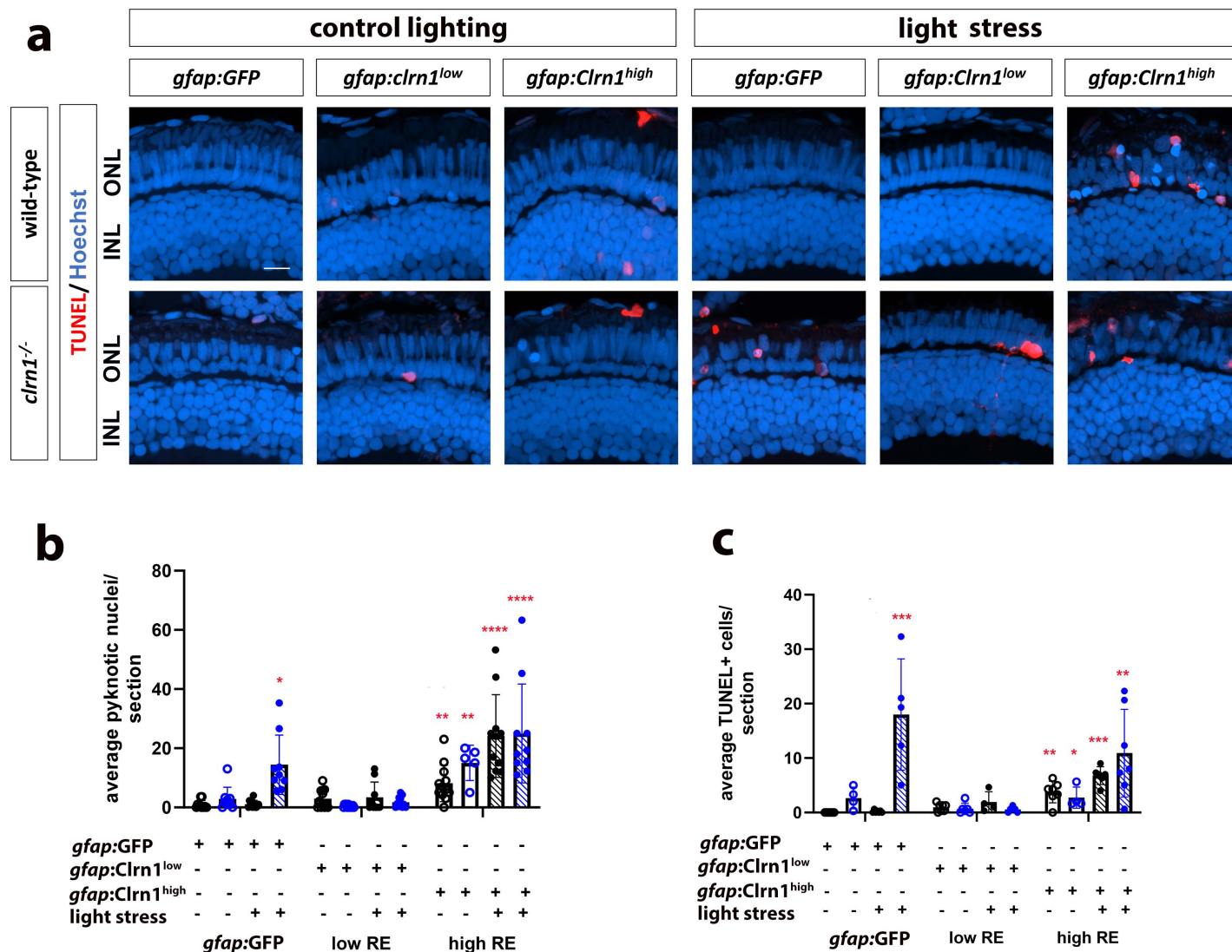


**Fig 10. Therapeutic efficacy of Clrn1 re-expression in Müller glia depends on expression level.** (a) Retinal images of 7 dpf wild-type (upper rows) and *clrn1*<sup>-/-</sup> mutant (lower rows) zebrafish expressing different transgenes (column labels) raised in control lighting conditions (right) or treated from 5–7 dpf with 3500 lux for 48 hours (left, light stress). Hoechst (blue) highlights nuclei of the outer (photoreceptor layer) and inner nuclear layers (labeled ONL and INL) while TUNEL staining (red) highlights dying cells. Quantitation of (b) pyknotic nuclei or (c) TUNEL-positive cells in the ONL reveals that the *gfap:Clrn1<sup>low</sup>* transgene decreases sensitivity to light stress induced cell death in *clrn1*<sup>-/-</sup> zebrafish while the *gfap:Clrn1<sup>high</sup>* transgene induced cell death in *clrn1*<sup>-/-</sup> and wild-type zebrafish. (\**p*<0.05, \*\**p*<0.01, \*\*\**p*<0.005, \*\*\*\**p*<0.001; Two-way ANOVA; Significance shown compared to wild-type *gfap:GFP* without light stress). Error bars=SD. Scale Bar = 50  $\mu$ m. *n*=8–12 larvae for each genotype per condition.

<https://doi.org/10.1371/journal.pgen.1011205.g010>

similar to those for the Müller glia *Clrn1* re-expression studies. In contrast to Müller glia specific re-expression of *Clrn1*, the rod or cone photoreceptors expressing *Clrn1* in a *clrn1*<sup>-/-</sup> mutant background were not protected against light stress (Figs 11 and 12).

## Discussion

In the current study, we developed a model of USH3A in zebrafish using a paired guide RNA-CRISPR-Cas9 strategy to delete the coding sequence of *clrn1*. This represents the first animal model of USH3 that displays photoreceptor degeneration, allowing us to investigate the impact of *Clrn1* absence on the retina and the cells that contribute to progressive vision

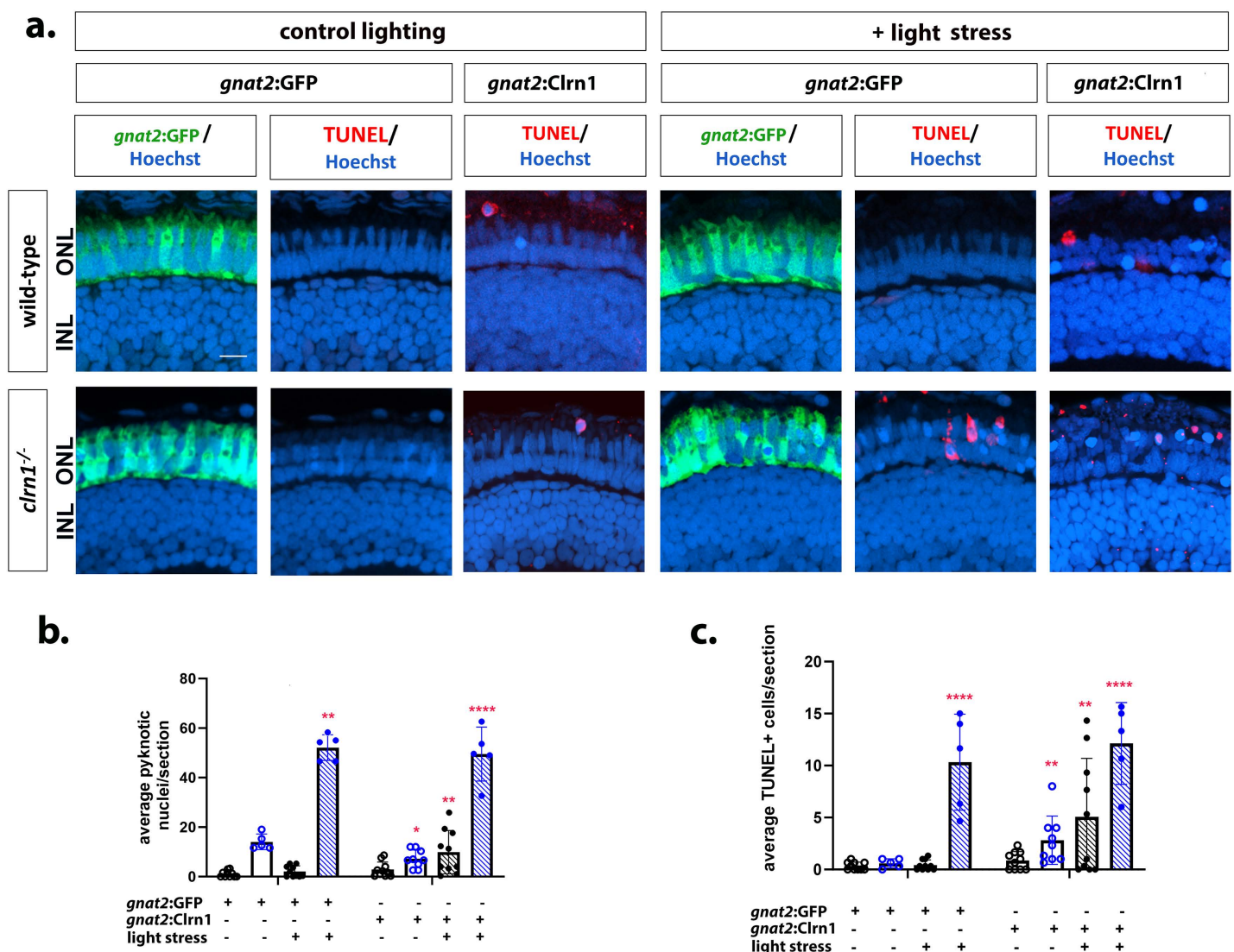


**Fig 11. Re-expression of *Clrn1* in cone photoreceptors does not reduce sensitive to light stress.** (a) Retinal images of 7 dpf wild-type (upper rows) and *clrn1*<sup>-/-</sup> mutant (lower rows) zebrafish expressing either *gnat2*:GFP or *gnat2*:*Clrn1* transgenes (column labels) raised in control lighting conditions (right) or treated from 5–7 dpf with 3500 lux for 48 hours (left, light stress). Hoechst (blue) highlights nuclei of the outer (photoreceptor layer) and inner nuclear layers (labeled ONL and INL) while TUNEL staining (red) highlights dying cells. Quantitation of (b) pyknotic nuclei or (c) TUNEL-positive cells in the ONL reveals that re-expression of *Clrn1* in cone photoreceptors does not protect *clrn1*<sup>-/-</sup> mutants from light stress induced cell death. (\**p*<0.05, \*\**p*<0.01, \*\*\**p*<0.005, \*\*\*\**p*<0.001; Two-way ANOVA; Significance shown compared to wild-type *gnat2*:GFP without light stress). Error bars=SD. Scale Bar = 50  $\mu$ m. *n*=5–10 larvae for each genotype per condition.

<https://doi.org/10.1371/journal.pgen.1011205.g011>



loss. Our results show that USH3A zebrafish retinas are sensitized to high-intensity light, and the cell death observed in the photoreceptor layer was due to loss of both rods and cones. In aging animals, we observed retinal dysfunction at the earliest time point investigated (4 mpf). In larval fish, differential therapeutic potentials were observed following the re-expression of *Clrn1* in Müller glia. Re-expression of *Clrn1* at relatively low levels in *clrn1* mutant Müller glia was associated with a reduction in photoreceptor apoptosis, underscoring the involvement of Müller glia in the pathophysiology of USH3A. Conversely, with high *Clrn1* expression, the therapeutic advantages were negated. Critically, this heightened expression of *Clrn1* in Müller glia induced the loss of photoreceptors in wild-type larvae and exacerbated the light stress induced photoreceptor cell death in *clrn1*<sup>-/-</sup> animals. This data provides important baseline knowledge to guide potential gene therapy initiatives.

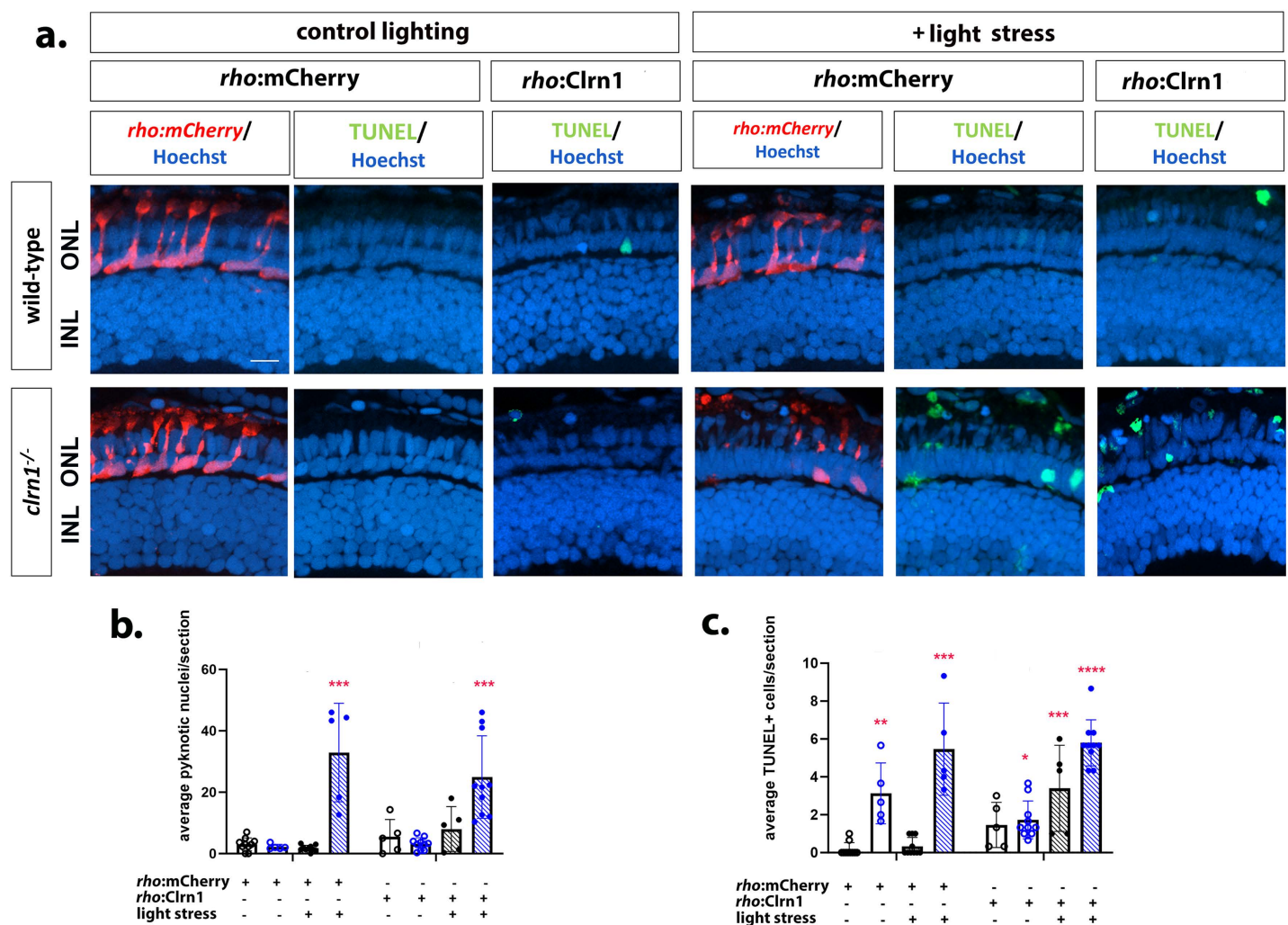


**Fig 12. Re-expression of *Clrn1* in rod photoreceptors does not reduce sensitive to light stress.** (a) Retinal images of 7 dpf wild-type (upper rows) and *clrn1*<sup>-/-</sup> mutant (lower rows) zebrafish expressing either *rho:GFP* or *rho:Clrn1* transgenes (column labels) raised in control lighting conditions (right) or treated from 5–7 dpf with 3500 lux for 48 hours (left, light stress). Hoechst (blue) highlights nuclei of the outer (photoreceptor layer) and inner nuclear layers (labeled ONL and INL) while TUNEL staining (red) highlights dying cells. Quantitation of (b) pyknotic nuclei or (c) TUNEL-positive cells in the ONL reveals that re-expression of *Clrn1* in rod photoreceptors does not protect *clrn1*<sup>-/-</sup> mutants from light stress induced cell death. (\**p* < 0.05, \*\**p* < 0.01, \*\*\**p* < 0.005, \*\*\*\**p* < 0.001; Two-way ANOVA; Significance shown compared to wild-type *rho:GFP* without light stress). Error bars=SD. Scale Bar = 50  $\mu$ m. *n*=5–10 larvae for each genotype per condition.

<https://doi.org/10.1371/journal.pgen.1011205.g012>

Unlike previously described *clrn1* mutant zebrafish, the *clrn1* mutants developed for this study survived into adulthood. Survival differences may be due to the genetic background, husbandry practices, or type of mutation. For our allele, we deleted 85% of the coding sequence, resulting in decay of the transcribed mRNA. For the previous USH3A zebrafish model, zinc finger nucleases were used to produce smaller deletions ranging from 7 bp to 43 bp within the first exon of the coding sequence [28]. While these mutations lead to the introduction of a premature stop codon, there are potential downstream start sites in subsequent exons, allowing for the potential expression of truncated proteins. Stop codon read-through is also possible. The expression of an altered Clrn1 protein could be more damaging to cells than complete loss of protein.

Consistent with previous reports on *clrn1* mutant zebrafish lines, in the absence of additional stressors, we did not observe any gross histological changes to the structure of the retina at 7 dpf. As others have done, we used high-intensity light treatment to enhance cellular stress on retinal cell types [15–17,55,56]. Following light stress, cell death was significantly increased in *clrn1*<sup>-/-</sup> zebrafish, as detected by pyknotic nuclei and TUNEL staining, which were elevated in both rods and cones. Within the peripheral and central retina, we observed a significant reduction in the number of rods and cones in *clrn1*<sup>-/-</sup> zebrafish. While this is the first report of *clrn1*<sup>-/-</sup> zebrafish presenting with a sensitivity to light damage, these findings are in accordance with other zebrafish models of USH [15–17], as well as other zebrafish models of retinitis pigmentosa that also show increased cell death following treatment with a high-intensity light [57,58].

In non-stressed conditions, we observed progressive functional and structural changes in the retina of *clrn1*<sup>-/-</sup> zebrafish, compared to their age-matched wild-type siblings. At 4 mpf, ERGs revealed rod and cone dysfunction. Interestingly, we did not observe a statistical difference in the average scotopic b-wave, but we did find greater variability in the scotopic B-wave of *clrn1*<sup>-/-</sup> zebrafish. Specifically, 30% of the animals presented with a hyper-response. At this same age, we observed an increase in BrdU-positive cells, which predominantly occurred in the region of the retina where the rod nuclei reside. Newly regenerated photoreceptors may affect the B-wave due to their immaturity or may promote circuit re-wiring as they integrate into the existing retina. At 4 mpf, we also observed a significant decrease in the photopic B-wave, implicating cone dysfunction. The decrease in the photopic ERG response could be due to the degeneration of cones or impaired cone function. Alternatively, Müller glia defects may affect opsin recycling or extracellular ion concentrations and account for differences in the scotopic and photopic responses. In mice, scotopic b-wave enhancements were observed during light-adapted ERGs early in the degenerative process of Rd10 (PDE6 mutant) mice [59,60]. In patients with cone dystrophy with supernormal rod response, patients present with elevated rod b-wave responses at higher light intensities, which is in agreement with the observations of hyper-responding *clrn1*<sup>-/-</sup> zebrafish [60–64]. However, the ERG presentation in *clrn1*<sup>-/-</sup> zebrafish deviates from the ERG recordings described for USH3A patients. In patients with USH3A, early ERG dysfunction begins with a reduced scotopic response and progresses to a reduced photopic response, as is typical of rod-cone dysfunction. The species differences in progression of ERG defects may be due to several reasons. These include (A) the more heterogeneous rod-to-cone composition across the human retina compared to the consistent ratios in zebrafish, (B) potential activation of regeneration in zebrafish, or (C) differential roles of Müller glia in retinoid recycling or contribution to the ERG.

Towards identifying a potential retinal function of *clrn1* and the pathological factors promoting retinal degeneration in USH3A, we focused on characterizing alterations in the actin-based structures in the outer retina. We found that the loss of Clrn1 leads to changes in the Müller glia apical microvilli and contacts between photoreceptors. The apical microvilli

projections appear more disorganized, with variable lengths, similar to reported stereocilia phenotypes of the inner ear of *clrn1* mutants [63]. These results are consistent with the function of *Clrn1* in actin organization and dynamics. In wild-type fish, the Müller glia projections appeared to envelop the base of the photoreceptor outer segments, suggesting structural support. Similar findings have also been recently highlighted recently [11]. We further described a close association between the Müller glia apical microvilli and cone calyceal processes (Fig 7). Our analysis of *clrn1*<sup>-/-</sup> mutants suggests that the association between Müller glia apical microvilli and photoreceptor calyceal processes, at least those of UV cones, might be mediated by *Clrn1*. It is possible this is through direct or indirect interaction between Müller glia expressed *Clrn1* and photoreceptor expressed USH-associated proteins. Additionally, alterations at the *clrn1* mutant OLM including N-cadherin distribution, are consistent with another role of Müller glia-derived *Clrn1* in mediating the integrity of the adherens junctions and thus providing additional structural support to photoreceptors. *Clrn1* function at the OLM may in part be mediated through interactions with N-cadherin, and Müller glia expressed USH-associated proteins, such as Harmonin. Defects observed in our *gfap:Clrn1*<sup>high</sup> transgenic animals, thus, may in part be a consequence of perturbing localization or activity of *Clrn1* binding partners that are essential to Müller glia functions.

Overall, our results suggest that *Clrn1* within Müller glia regulates the architecture of Müller glia and non-autonomously maintains photoreceptor homeostasis. Future studies aimed at the identifying *Clrn1*-binding partners within Müller glia could assist in better defining precise cellular mechanisms. Importantly, these findings suggest gene replacement therapy for USH3A patients holds promise, but the dosage and timing of *CLRN1* expression within Müller glia must be carefully evaluated.

## Materials and methods

### Ethics statement

All animal experiments were approved by the Institutional Animal Care and Use Committee of the Medical College of Wisconsin.

### Zebrafish maintenance

All transgenic and mutant lines were generated and maintained in the ZDR genetic background. When possible and if otherwise not noted, wild-type siblings or cousins of each line were used as control groups. Zebrafish (*Danio rerio*) were maintained at 28.5°C on an Aquatic Habitats recirculating filtered water system (Aquatic Habitats, Apopka, FL) in reverse-osmosis purified water supplemented with Instant Ocean salts (60mg/l) on a 14 h light: 10 h dark lighting cycle and fed a standard diet.

### Generation of *clrn1* mutant zebrafish

Due to the small size of *clrn1* (ENSDART00000171202.2), 85% of the coding sequence was deleted using a gRNA targeting Exon1 (5'-CTCGACTCAGTTTTGGGTTCAAGC-3') and another gRNA targeting the 3'UTR (5'-AGCTCGCTTAAGCCATTGAGAGCA-3'). gRNAs were purchased from IDT (Coralville, IA) and processed according to manufacturer instructions. For the generation of *clrn1* mutant lines, gRNAs (10 ng/μl) and Cas9 protein was co-injected into 1- to 4-cell wild-type zebrafish embryos (ZDR strain). Surviving embryos were raised to adulthood before outcrossing to identify the founder fish carrying germline edits in *clrn1*. Offspring from these fish were raised to adulthood, thereafter, fin-clipped for genotyping. The resulting deletion was confirmed via sequencing (Retrogen, San Diego, California, USA).



## Genotyping

Genomic DNA was extracted from zebrafish tissue using a Puregene Core Kit (Qiagen, Germantown, MD). The genomic region containing the desired large deletion was amplified using primers external to each cut site. For detection of the mutant band the forward primer sequence used 5'-GTTTCATATATTCAGGCGTGC-3' and the reverse primer sequence used was 5'-AGAGGAAACTGTGATGTCCC-3'. The thermocycler conditions for detecting the presence of a large deletion allele were designed using extension times, allowing only the amplification of the mutant region. When detecting the presence of a wild-type allele a third internal primer located within the sequence deleted was. The sequence for the internal reverse primer was 5'-AGTTGGGTTTAGGTTTGGGTAG-3'. For genotyping *Tg(gfap:Clrn1<sup>low</sup>)* larvae on a *Tg(gfap:GFP)* background, the following primers were used: 5'-CGCCTGCTTGGTCCTCATTT-3' and 5'-ACAGAGAGAAGTTCGTGGCT-3'.

## RNA extraction and amplification of *clrn1* cDNA

For mRNA isolation, samples were homogenized in Trizol (ThermoFisher, Waltham, MA) followed by mRNA extraction using Trizol-chloroform treatment. The isolated aqueous phase from the resulting Trizol-chloroform phase separation was transferred to a new tube and incubated with isopropanol and glycogen at room temperature for 10 minutes. Samples were centrifuged at 4°C for 10 minutes to pellet the precipitated RNA. Isolated RNA was washed with 75% ethanol in DEPC-treated water. Following this wash, the pellet was briefly dried then resuspended in DEPC-treated water with a 10-minute incubation at 60°C. Resuspended RNA is then subjected to a DNase I treatment, and concentration was quantified. cDNA was generated using the Superscript III First-Strand Synthesis System for RT-PCR Kit (Invitrogen, Waltham, MA) per manufacturer's instructions and all qRT-PCR was performed on a CFX Connect Real-Time System (Bio-Rad, Hercules, CA) using prime time gene expression master mix (IDT).

## Plasmid construction

Plasmids were constructed using Gateway assembly (Thermo Fisher Scientific, Waltham, MA). The pME' *clrn1* entry clone was generated by amplifying the full-length cDNA of *clrn1* (ENS-DART00000171202.2) with primers containing attB recombination sites (Clrn1 attB2 FPrimer: 5'-GGGGACAAGTTTGTACAAAAAAGCAGGCTCCATGCCTAACCGTCAAAAGCA-3'

Clrn1 attB3 FPrimer: 5'-GGGGACCACTTTGTACAAGAAAGCTGGGTCGTACAT-GAGATCTGCAGCTC-3')

and placed into a pME' entry clone. The *gfap:Clrn1-2A-GFP*, *rho:Clrn1-2a-mCherry*, and *gnat2:Clrn1-2A-mCherry* plasmids were generated using the three-part Gateway system. Specifically, the pME' *clrn1* was recombined with respective cell-specific p5E' plasmids (Müller glia: *gfap*, rod photoreceptors: *rho*, cone photoreceptors: *gnat2*) and p3E' 2A-GFP. The backbone vector contained Tol-2-inverted repeats flanking the transgene construct, which were used to facilitate plasmid insertion into the zebrafish genome [63]. Similarly, the control plasmids (*gfap:GFP*, *rho:mCherry*, and *gnat2:GFP*) were generated using a p5E'*gfap* promoter, pME' eGFP or pME'mCherry, and p3E' polyA into a backbone vector with Tol-2 inverted repeats. For analysis of cone photoreceptor actin structures, a pME-Lifeact [65] plasmid was a gift from Rob Parton (Addgene plasmid #109545). Using gateway cloning, this was recombined with a p5E' *gnat2* promoter and p3' mCherry into a backbone vector with Tol-2 inverted repeats.

## Generation of transgenic lines

To generate transgenic zebrafish, transposase mRNA (10 ng/ul) was injected with plasmid DNA (10 ng/ul) to generate F0 transgenic lines. F0 fish were screened for reporter fluorescence in the Müller glia. Expressing F0 fish were raised to adulthood and outcrossed to establish F1 transgenic zebrafish with germline integration of the transgene. F1 transgenic larvae were raised to adulthood and outcrossed to wild-type zebrafish. Clutches with around 50% of F2 embryos with reporter expression were identified, suggesting a single active copy of the transgene were used for subsequent analysis.

## Mutant and transgenic alleles generated in this study

*clarin1*<sup>mw99</sup>

Tg(*gfap*:Clrn1-2A-GFP<sup>low</sup>)<sup>mw100Tg</sup>

Tg(*gfap*:Clrn1-2A-GFP<sup>high</sup>)<sup>mw102Tg</sup>

Tg(*rho*:Clrn1-2A-mCherry)<sup>mw103Tg</sup>

Tg(*gnat2*:Clrn1-2A-mCherry)<sup>mw104Tg</sup>

Tg(*gfap*:GFP)<sup>mw105Tg</sup>

Tg(*rho*:mCherry)<sup>mw106Tg</sup>

Tg(*gnat2*:GFP)<sup>mw107Tg</sup>

Tg(*gnat2*:LIFEACT-mCherry)<sup>mw108Tg</sup>

## Fluorescent marker analysis

To prepare larvae for cryosections, animals were anesthetized with 0.016% tricaine methanesulfonate and fixed overnight at 4°C in 4% PFA. Following fixation, larvae were washed three times for 10 minutes with PBS. Larvae were subsequently stepped through a sucrose gradient and incubated in OCT compound (Optimum Cutting Temperature medium) overnight. Following overnight incubation in OCT compound animals were mounted in OCT compound, frozen on dry ice, and then stored in the -80°C until sectioned. For staining, retinal cryosections were treated with PBST (PBS with 0.1% Triton 100) for one hour, then incubated in blocking solution containing 5% normal goat serum for one hour. Primary antibody was diluted in PBST containing 5% normal goat serum (NGS), and sections were incubated overnight at 4°C. Following washes in PBST, sections were stained with secondary, diluted in PBST containing 2% normal goat serum. For phalloidin staining, sections or whole mount preparations were pre-incubated in PBST for one hour. Samples were stained for one hour with phalloidin Alexa fluor 488 (1:300, ThermoFisher, A12379) or phalloidin Alexa fluor 568 (1:300, ThermoFisher, A12380). For PNA and WGA staining, animals were stained before sectioning. Specifically, animals were treated with PBST for one hour, followed by 4 hours of staining with rhodamine conjugated PNA (1:250, Vector Labs RL 1072) and WGA alexa fluor 488 (1:250, ThermoFisher, W11261) or WGA Alexa fluor 594 (1:250, ThermoFisher, W11262). Larvae were then washed with PBS and processed as discussed above. For all staining, samples were counter stained with Hoechst (1:1000, ThermoFisher, 62249). Slides were cover slipped with Vectashield (Vector Labs, H-1000) and analyzed by confocal microscopy.

## Paraffin histology

Adult fish used for paraffin histology were fixed in 10% neutral buffer formalin overnight at 4°C. Prior to fixation, heads were bisected to allow for better fixation of the retina. Samples were then mounted in histogel and processed in paraffin on a Sakura VIP5 automated tissue processor (Sakura Finetek Europe, Flemington, The Netherlands) for histology and immunohistochemistry. After paraffin embedding, samples were sectioned at 4 µm (Microm HM355S, ThermoFisher Scientific, Waltham, Massachusetts, USA) onto poly-L-lysine coated slides and air-dried at 45°C overnight for any subsequent immunohistochemistry or routine H&E staining.

## Immunohistochemistry - paraffin sections

All slides were dewaxed prior to their optimal antigen retrieval protocol. All antibodies used a citrate buffer epitope retrieval (DAKO, Agilent). Slides were washed in PBST to remove excess retrieval buffer. Slides were blocked for one hour in PBST with 5% NGS. Samples were incubated with primary antibodies overnight at 4°C. After primary, slides were washed in PBS, then incubated with secondary antibodies (1:500) diluted in PBST with 2% NGS. Slides were washed in PBS then counterstained with Hoechst (1:1000, ThermoFisher, 62249) for 15 min. Sections were protected with Vectashield mounting medium (Vector Labs, H-1000).

## RNAscope *in situ* hybridization

*In situ* hybridization (ISH) was performed on paraffin-embedded zebrafish retina sections. *Cln1* transcripts were detected using an automated Leica Bond platform with heat-induced Leica ER2 antigen retrieval buffer solution and RNAscope 2.5 LS Protease III digestion (Advanced Cell Diagnostics, Hayward, CA, USA), as previously described [32]. Briefly, after hybridization to 20ZZ probes targeting the region comprising nucleotides 2-911 of Dr-cln1 NM\_001002671.1, a six-step amplification process was performed, followed by chromogenic detection using Fast Red (Advanced Cell Diagnostics). Images were collected with a fully automated widefield DMi8 Leica fluorescence microscope.

## Antibodies

Anti-BrdU was purchased from Abcam (Rat monoclonal, ab6326) and used at a dilution of 1:300 for the staining of paraffin sections. Anti-espina was purchased from Sigma-Aldrich (rabbit polyclonal, HPA028674) and used at 1:500 for cryosections. Anti-Cdh2 (N-cadherin) was purchased from GeneTex (GTX125962) and used at 1:500 for cryosections. Zpr3 monoclonal antibody (recognizing zebrafish Rhodopsin and green opsin, [66]) was purchased from the Developmental Studies Hybridoma Bank and used at 1:200 for cryosections. The secondary antibodies used for immunofluorescent detection were goat anti-rat secondary Alexa fluor 488 (ThermoFisher A-11006), goat anti-rabbit secondary Alexa fluor 568 (ThermoFisher, A-11011), goat anti-mouse secondary Alexa fluor 568 (ThermoFisher A-32742).

## Fluorescent microscopy

Confocal microscopy was performed using a Nikon Eclipse E800, C2 Nikon Eclipse 80i, or Zeiss LSM 980 confocal microscope. For whole mount imaging, larvae were embedded in 1% low-melting agarose in glass-bottomed Petri dishes. Images were generated using ImageJ software (Rasband, W.S. ImageJ, U.S. National Institutes of Health, MD).



### Spectral domain – optical coherence tomography (SD-OCT)

Zebrafish eyes were imaged using a Biophtigen Envisu R2310 SD-OCT imaging system, equipped with a 12 mm telecentric lens (Biophtigen, Morrisville, NC) using a Superlum Broad-lighter T870 light source centered at 878.4 nm with a 186.3 nm band width (Superlum, Cork, Ireland). Volume scans were nominally  $1.0 \times 1.0$  mm with isotropic sampling (500 A scans/B scan; 500 B scans). Raw OCT scans for retinal images were exported and processed using a custom OCT volume viewer (Java software, Oracle Corporation, Redwood Shores, CA), in which an adjustable contour is used to generate *en face* summed volume projection (SVP) images (66,67). For a given B-scan, 15 control points were added to the initial contour, where each control point is adjusted to follow the contour of the layer(s) of interest. Multiple *en face* images can be generated for each OCT volume, resulting in images of different retinal features (e.g., inner retinal vasculature and photoreceptor mosaic). *En face* images of the NFL, RPE, and UV cones were generated to visualize the cone mosaic, RPE pigmentation, and gaps in the reflectivity of the NFL [67]. Using *en face* images of the UV cone mosaic, mosaic geometry were assessed from the resultant cone coordinates using a custom program as previously described [40].

### Optomotor reflex (OMR) assay

The OMR assay was performed on 7dpf larvae that were maintained in standard lighting conditions or treated with high-intensity light from 5–7 dpf. To test for OMR, larvae were placed in a 48-well plate placed on top of a tablet playing the stimulation videos. Animals were recorded for a three-minute period with direction changes at 1-minute intervals. Animals were scored on their ability to detect direction changes within the first 10 seconds. Zebrafish that could not be tracked for all three passes were not included in the analysis. Stimulation used for assay was generated using publicly available software developed by Brastrom *et al* [68].

### BrdU treatment

To assess for regeneration, BrdU labeling was performed to label newly generated cells in the adult zebrafish retina. Prior to collection, adult animals were placed in fish water containing 10 mM 5-bromo-2'-deoxyuridine (BrdU) (Abcam, Cambridge, UK) overnight 1 and 2 weeks before animals were sacrificed. After treatment, animals were rinsed twice for 10 min in fresh fish water to rinse off excess BrdU.

### TUNEL staining

TUNEL technique using the *in-situ* cell death detection kit, Roche (Millipore Sigma CA, USA), was performed according to the manufacturer's instructions on cryosectioned samples. For staining, slides were incubated in PBST for one hour (PBS with 1% TritonX-100). Following PBST, the samples were incubated at 37°C with the TUNEL reaction mixture (containing 5 µl of TdT + 45 µl of fluorescein conjugated dUTP) for two hours. Following incubation in TUNEL mixture, samples were washed for 30 minutes in 1X PBST. Slides were co-stained with Hoechst for 15 min, then washed 3 times for 10 min in PBST. The number of TUNEL positive cells were manually counted and averaged across three sections in the central retina.

### Histology and transmission electron microscopy

7 dpf larvae were fixed with 1.0% paraformaldehyde, 2.5% glutaraldehyde in 0.06-M cacodylate buffer (pH 7.4) overnight at 4°C. Post fixation, samples were washed in cacodylate buffer and post-fixed with 1% osmium tetroxide and then dehydrated by a series of methanol and

acetonitrile washes. Larvae were infused with Epon 812 resin (Electron Microscopy Sciences, Hatfield, PA, USA) incubating with 1:1 acetonitrile:Epon for one hour, followed by an incubation in 100% Epon in a 37°C degree water bath, then 100% Epon in a 37°C heat block. Finally, larvae were embedded in 100% Epon and hardened at 65°C for 24 hours. For transmission electron microscopy (TEM) analysis, 70-nm sections were cut, collected on hexagonal grids, and stained with uranyl acetate and lead citrate for contrast, followed by imaging on a Hitachi H-600 Transmission Electron Microscope (Hitachi, Ltd., Tokyo, Japan).

### *Ex Vivo* electroretinograms

*Ex vivo* ERGs were performed using the OcuScience (Henderson, Nevada) *Ex Vivo* ERG adapter according to previous published protocols, with appropriate modifications for analysis of zebrafish retinal function [69]. Prior to performing ERGs, animals were dark adapted overnight, and all experimental setups were performed under dim red illumination. Zebrafish were anesthetized in 0.016% tricaine methanesulfonate. Once anesthetized, optic cups were dissected in AMES media (A1420, Sigma-Aldrich, CA, USA). To dissect optic cups, eyes were punctured with a 28-gauge needle. Two forceps were used to peel off the sclera and RPE. During this process the lens was also removed. Samples were then mounted in the *ex vivo* ERG adaptor. During recording, samples were perfused with AMES media at a rate of 5–10 ml/hr. ERG recordings were carried out using an Espion E2 system (Diagnosys LLC, Cambridge, UK) with a low frequency filter of 0 Hz, high frequency filter of 1000 Hz, and notch filter of 60 Hz (Bessel filters). The scotopic session included a single flash stimulus increasing from 0.1 mcDs/m<sup>2</sup> to 25 cDs/m<sup>2</sup>. Six response per intensity level were averaged, with an inter-stimulus interval of 5 seconds for stimuli ranging from 0.1 mcDs/m<sup>2</sup> to 100 mcDs/m<sup>2</sup>. For stimuli above 100 mcDs/m<sup>2</sup>, an inter-stimulus interval of 17 seconds was used. For the photopic session animals were light adapted for 10 min with a background illumination of 30 cd/m<sup>2</sup>. Following the light adaptation of 10 min, the photopic session began with single flash recordings as above but with a reduced number of light intensities (0.03, 0.1, 1, 3, 10 and 25 cDs/m<sup>2</sup>). Subsequently, flicker ERGs were obtained with flashes of 3 cDs/m<sup>2</sup> using frequencies of 1, 2, 5, 10, 15, 20, 25 and 30 Hz. During recording, all equipment was located within a Faraday cage to minimize external electrical noise.

### Masking prior to analysis

Quantification for at least one experimental group of each data set was masked. Masking was done by either coding tanks (OCT), image files (histology), or slides (fluorescent images) until they were through sectioning, staining, imaging, and/or scoring.

### Statistical analysis

Mean or total pixel intensity was measured using ImageJ (Rasband, W.S. ImageJ, U.S. National Institutes of Health, MD). Data was processed using Microsoft Excel (Microsoft, Redmond, WA) and graphed using GraphPad Prism (GraphPad, La Jolla, CA). An unpaired, two-tailed t test was used to analyze graphs with two groups. For three or more groups, a one-way or two-way ANOVA was conducted with Tukey's post-hoc analysis for pair-wise comparisons.

### Supporting information

#### **S1 Fig. Method to genotype for *clarin1*<sup>-/-</sup>, wild-type, and heterozygous zebrafish. (a)**

Overview of genotyping assay to identify wild-type, *clarin1*<sup>+/-</sup>, and *clarin1*<sup>-/-</sup> zebrafish. A common forward primer (C-FP) was designed upstream of the exon 1 cut site, while a mutant reverse primer (M-RP) was designed downstream of the 3' UTR cut site, and wild-type reverse primer

(W-RP) was designed internal to the exon 1 cut site. (b) Generation of the large deletion in the *clrn1* coding sequence was confirmed with Sanger sequencing. (c) Example gel depicting the PCR amplification products for wild-type, *clrn1*<sup>-/-</sup>, and *clrn1*<sup>+/-</sup> (het) zebrafish.

(TIFF)

**S2 Fig. Representative traces of photopic and scotopic responses.** Representative traces from four 4 mpf wild-type (black traces) and *clrn1*<sup>-/-</sup> (blue traces) (a) scotopic and (b) photopic responses to highlight high variability in the *clrn1*<sup>-/-</sup> scotopic b-wave. Representative traces from 12 mpf wild-type and *clrn1*<sup>-/-</sup> (c) scotopic and (d) photopic responses.

(TIFF)

**S3 Fig. Photopic flicker response are reduced in 4 and 12 mpf *clrn1*<sup>-/-</sup> zebrafish.** Representative photopic flicker traces of 4 and 12 mpf wild-type (black traces) and *clrn1*<sup>-/-</sup> (blue traces) at a range of 1-30 hz.

(TIFF)

**S4 Fig. Scotopic and photopic B-wave implicit times at 4 and 12 mpf.** (a) Scotopic and (c) photopic b-wave implicit time for wild-type and *clrn1*<sup>-/-</sup> zebrafish at 4 mpf. (b) Scotopic and (d) photopic b-wave implicit time for wild-type and *clrn1*<sup>-/-</sup> zebrafish at 12 mpf. (\*p<0.05; \*\*\*p<0.001; One-way ANOVA) (n=10 animals/eyes per genotype for each time-point). Error bars=SD.

(TIFF)

**S5 Fig. BrdU incorporation is elevated in *clrn1*<sup>-/-</sup> zebrafish at 4 mpf and decreases with age.** Anti-BrdU (green) staining in paraffin sections from (a,a') 4 mpf, (b,b') 8 mpf, (c,c') 12 mpf, and (d,d') 20 mpf in wild-type and *clrn1*<sup>-/-</sup> zebrafish retinas. Quantification of BrdU+ nuclei in the (e) outer nuclear layer (ONL, or Photoreceptor layer) and (f) inner nuclear layer (INL) revealed an increase in BrdU incorporation for *clrn1*<sup>-/-</sup> zebrafish at the youngest time point which decreased with age. White arrows highlight BrdU+ nuclei. (\*p<0.05; \*\*p<0.01; One-way ANOVA). Scale bar=10 μm. Data points are averages of 3 sections per retina. n=10 retina per genotype for each time-point.

(TIFF)

**S6 Fig. OMR responses in wild-type and *clrn1*<sup>-/-</sup> zebrafish maintained in standard or high-intensity light conditions 5 to 7 dpf.** (a) Distribution of OMR responses (number of positive movements in response to 3 direction changes of the moving striped pattern) in wild-type and *clrn1*<sup>-/-</sup> control or with light stress (+LS) zebrafish. (b) Representative images of wild-type (upper) and *clrn1*<sup>-/-</sup> (lower) larva positions (red arrows) following stimulus direction change (blue arrows indicate direction of moving stripes).

(TIFF)

**S7 Fig. Colocalization of *gnat2*:Lifeact-mCherry fluorescence and Espn immunoreactivity.** Wild-type 7 dpf larvae were used to investigate whether enriched signal from (a) cone photoreceptor specific Lifeact-mCherry (red) is from calyceal processes marked by (b) Espn immunoreactivity (magenta). (c) Merged images demonstrate significant overlap. Müller glia processes from Tg(*gfap:gfp*) are shown in green for each image. Hoechst staining (blue) in (c) labels photoreceptor nuclei. Scale bar = 5 μm. OS, Outer Segment; IS, Inner Segment; OLM, Outer limiting membrane; ONL, Outer nuclear layer.

(TIFF)

**S8 Fig. Analysis of photoreceptor junction by transmission electron microscopy.** Representative TEM micrographs of the photoreceptor junctions for wild-type and *clrn1*<sup>-/-</sup> at 7dpf. White Boxes highlight cell junctions in the OLM. Scale Bar = 1 mm.

(TIFF)



**S9 Fig. Expression level difference between Clrn1 high and low re-expression in Müller glia transgenic lines.** (a) Diagram of Müller glia specific Clrn1 expression transgene (b) Images of the *Tg(gfap:Clrn1<sup>low</sup>)* and *Tg(gfap:Clrn1<sup>high</sup>)* at a lower and a higher gain to show the low-level reporter expression in the *gfap:Clrn1<sup>low</sup>* line. (c). Quantification of total GFP fluorescence intensity in the *Tg(gfap:Clrn1<sup>low</sup>)* and *Tg(gfap:Clrn1<sup>high</sup>)* lines within the retina. (\*\*\*\* $p < 0.001$ ; Unpaired Students T-test).  $n = 10$  zebrafish for each transgenic line. (TIFF)

**S10 Fig. Analysis of outer retina structures in clrn1<sup>-/-</sup> mutants with and without re-expression of Clrn1 in Müller glia.** Comparison of Müller glia morphology and actin organization within the outer retina in (a) wild-type, (a) clrn1<sup>-/-</sup> mutants alone, (c), clrn1<sup>-/-</sup> mutants with *Tg(gfap:Clrn1<sup>low</sup>)*, and (d) clrn1<sup>-/-</sup> mutants with *Tg(gfap:Clrn1<sup>high</sup>)*. Comparisons reveal that re-expression Clrn1 in clrn1<sup>-/-</sup> mutants with the *Tg(gfap:Clrn1<sup>low</sup>)* transgene corrects disorganization of apical microvilli projections and actin in the outer retina, while re-expression Clrn1 in clrn1<sup>-/-</sup> mutants with the *Tg(gfap:Clrn1<sup>high</sup>)* transgene exacerbates disorganization of these structures. Scale Bar = 50  $\mu\text{m}$ . OLM, Outer Limiting Membrane; IPL, Inner Plexiform Layer.  $n = 10$ -15 zebrafish per group. (TIFF)

**S1 Data. Quantitative data for Fig 2.**  
(XLSX)

**S2 Data. Quantitative data for Fig 3.**  
(XLSX)

**S3 Data. Quantitative data for Fig 4.**  
(XLSX)

**S4 Data. Quantitative data for Fig 5.**  
(XLSX)

**S5 Data. Quantitative data for Fig 6.**  
(XLSX)

**S6 Data. Quantitative data for Fig 9.**  
(XLSX)

**S7 Data. Quantitative data for Fig 10.**  
(XLSX)

**S8 Data. Quantitative data for Fig 11.**  
(XLSX)

**S9 Data. Quantitative data for Fig 12.**  
(XLSX)

## Author contributions

**Conceptualization:** Hannah J. T. Nonarath, Ross F. Collery, Astra Dinculescu, Brian A Link.

**Data curation:** Hannah J. T. Nonarath.

**Formal analysis:** Hannah J. T. Nonarath, Astra Dinculescu, Brian A Link.

**Funding acquisition:** Ross F. Collery, Astra Dinculescu, Brian A Link.

**Investigation:** Hannah J. T. Nonarath, Samantha L. Simpson, Tricia L. Slobodianuk, Hai Tran.

**Methodology:** Hannah J. T. Nonarath, Ross F. Collery, Astra Dinculescu, Brian A Link.

**Project administration:** Brian A Link.

**Supervision:** Ross F. Collery, Astra Dinculescu, Brian A Link.

**Validation:** Hannah J. T. Nonarath, Samantha L. Simpson, Tricia L. Slobodianuk.

**Visualization:** Hannah J. T. Nonarath, Brian A Link.

**Writing – original draft:** Hannah J. T. Nonarath, Brian A Link.

**Writing – review & editing:** Hannah J. T. Nonarath, Samantha L. Simpson, Tricia L. Slobodianuk, Hai Tran, Ross F. Collery, Astra Dinculescu, Brian A Link.

## References

1. Ben-Rebeh I, Grati M, Bonnet C, Bouassida W, Hadjamor I, Ayadi H, et al. Genetic analysis of Tunisian families with Usher syndrome type 1: toward improving early molecular diagnosis. *Molecular Vision*. 2016;22:827–35.
2. Boughman JA, Vernon M, Shaver KA. Usher syndrome: definition and estimate of prevalence from two high-risk populations. *J Chronic Dis*. 1983;36(8):595–603. [https://doi.org/10.1016/0021-9681\(83\)90147-9](https://doi.org/10.1016/0021-9681(83)90147-9) PMID: 6885960
3. Vernon M. Usher's syndrome--deafness and progressive blindness. Clinical cases, prevention, theory and literature survey. *J Chronic Dis*. 1969;22(3):133–51. [https://doi.org/10.1016/0021-9681\(69\)90055-1](https://doi.org/10.1016/0021-9681(69)90055-1) PMID: 4897966
4. Stiff HA, Sloan-Heggen CM, Ko A, Pfeifer WL, Kolbe DL, Nishimura CJ, et al. Is it Usher syndrome? Collaborative diagnosis and molecular genetics of patients with visual impairment and hearing loss. *Ophthalmic Genet*. 2020;41(2):151–8. <https://doi.org/10.1080/13816810.2020.1747088> PMID: 32281467
5. Calabro KR, Boye SL, Choudhury S, Fajardo D, Peterson JJ, Li W, et al. A Novel Mouse Model of MYO7A USH1B Reveals Auditory and Visual System Haploinsufficiencies. *Front Neurosci*. 2019;13:1255. <https://doi.org/10.3389/fnins.2019.01255> PMID: 31824252
6. Tian C, Liu X, Han F, Yu H, Longo-Guess C, Yang B. Ush1c gene expression levels in the ear and eye suggest different roles for Ush1c in neurosensory organs in a new Ush1c knockout mouse. *Brain Research*. 2010;1328:57–70.
7. Geller SF, Guerin KI, Visel M, Pham A, Lee ES, Dror AA, et al. CLRN1 is nonessential in the mouse retina but is required for cochlear hair cell development. *PLoS Genet*. 2009;5(8):e1000607. <https://doi.org/10.1371/journal.pgen.1000607> PMID: 19680541
8. Sahly I, Dufour E, Schietroma C, Michel V, Bahloul A, Perfettini I, et al. Localization of Usher 1 proteins to the photoreceptor calyceal processes, which are absent from mice. *J Cell Biol*. 2012;199(2):381–99. <https://doi.org/10.1083/jcb.201202012> PMID: 23045546
9. Trouillet A, Dubus E, Dégardin J, Estivalet A, Ivkovic I, Godefroy D, et al. Cone degeneration is triggered by the absence of USH1 proteins but prevented by antioxidant treatments. *Sci Rep*. 2018;8(1):1968.
10. Sharkova M, Chow E, Erickson T, Hocking JC. The morphological and functional diversity of apical microvilli. *J Anat*. 2023;242(3):327–53. <https://doi.org/10.1111/joa.13781> PMID: 36281951
11. Sharkova M, Aparicio G, Mouzaaber C, Zolessi FR, Hocking JC. Photoreceptor calyceal processes accompany the developing outer segment, adopting a stable length despite a dynamic core. *J Cell Sci*. 2024;137(7):jcs261721. <https://doi.org/10.1242/jcs.261721> PMID: 38477343
12. Liu X, Vansant G, Udovichenko IP, Wolfrum U, Williams DS. Myosin VIIa, the product of the Usher 1B syndrome gene, is concentrated in the connecting cilia of photoreceptor cells. *Cell Motil Cytoskeleton*. 1997;37(3):240–52. [https://doi.org/10.1002/\(sici\)1097-0169\(1997\)37:3<240::aid-cm6>3.0.co;2-a](https://doi.org/10.1002/(sici)1097-0169(1997)37:3<240::aid-cm6>3.0.co;2-a)
13. Nagel-Wolfrum K, Fadl BR, Becker MM, Wunderlich KA, Schäfer J, Sturm D, et al. Expression and subcellular localization of USH1C/harmonin in human retina provides insights into pathomechanisms and therapy. *Hum Mol Genet*. 2023;32(3):431–49. <https://doi.org/10.1093/hmg/ddac211> PMID: 35997788
14. Phillips JB, Blanco-Sanchez B, Lentz JJ, Tallafuss A, Khanobdee K, Sampath S, et al. Harmonin (Ush1c) is required in zebrafish Müller glial cells for photoreceptor synaptic development and function. *Dis Model Mech*. 2011;4(6):786–800. <https://doi.org/10.1242/dmm.006429> PMID: 21757509
15. Miles A, Blair C, Emili A, Tropepe V. Usher syndrome type 1-associated gene, pcdh15b, is required for photoreceptor structural integrity in zebrafish. *Dis Model Mech*. 2021;14(12):dmm048965. <https://doi.org/10.1242/dmm.048965> PMID: 34668518

16. Wasfy M, Matsui J, Miller J, Dowling J, Perkins B. myosin 7aa<sup>-/-</sup> mutant zebrafish show mild photoreceptor degeneration and reduced electroretinographic responses. *Experimental Eye Research*. 2014;122:65–76.
17. Dona M, Slijkerman R, Lerner K, Broekman S, Wegner J, Howat T, et al. Usherin defects lead to early-onset retinal dysfunction in zebrafish. *Exp Eye Res*. 2018;173:148–59. <https://doi.org/10.1016/j.exer.2018.05.015> PMID: 29777677
18. Toms M, Dubis AM, de Vrieze E, Tracey-White D, Mitsios A, Hayes M, et al. Clinical and preclinical therapeutic outcome metrics for USH2A-related disease. *Hum Mol Genet*. 2020;29(11):1882–99. <https://doi.org/10.1093/hmg/ddaa004> PMID: 31998945
19. Joensuu T, Hämäläinen R, Yuan B, Johnson C, Tegelberg S, Gasparini P, et al. Mutations in a novel gene with transmembrane domains underlie Usher syndrome type 3. *Am J Hum Genet*. 2001;69(4):673–84. <https://doi.org/10.1086/323610> PMID: 11524702
20. Adato A, Vreugde S, Joensuu T, Avidan N, Hamalainen R, Belenkiy O, et al. USH3A transcripts encode clarin-1, a four-transmembrane-domain protein with a possible role in sensory synapses. *Eur J Hum Genet*. 2002;10(6):339–50. <https://doi.org/10.1038/sj.ejhg.5200831> PMID: 12080385
21. Marouf A, Johnson B, Alagramam KN. Usher syndrome IIIA: a review of the disorder and preclinical research advances in therapeutic approaches. *Human Genetics*. 2022;141(3–4):759–83.
22. Ness SL, Ben-Yosef T, Bar-Lev A, Madeo AC, Brewer CC, Avraham KB, et al. Genetic homogeneity and phenotypic variability among Ashkenazi Jews with Usher syndrome type III. *J Med Genet*. 2003;40(10):767–72. <https://doi.org/10.1136/jmg.40.10.767> PMID: 14569126
23. Dinculescu A, Link B, Saperstein D. Retinal gene therapy for Usher syndrome: Current developments, challenges, and perspectives. *International Ophthalmology Clinics*. 2021;61(4):109–24.
24. Tian G, Lee R, Ropelewski P, Imanishi Y. Impairment of Vision in a Mouse Model of Usher Syndrome Type III. *Invest Ophthalmol Vis Sci*. 2016;57(3):866–75. <https://doi.org/10.1167/iov.15-16946> PMID: 26943149
25. Phillips JB, Västinsalo H, Wegner J, Clément A, Sankila E-M, Westerfield M. The cone-dominant retina and the inner ear of zebrafish express the ortholog of CLRN1, the causative gene of human Usher syndrome type 3A. *Gene Expr Patterns*. 2013;13(8):473–81. <https://doi.org/10.1016/j.gexp.2013.09.001> PMID: 24045267
26. Isosomppi J, Västinsalo H, Geller S, Heon E, Flannery J, Sankila E. Disease-causing mutations in the CLRN1 gene alter normal CLRN1 protein trafficking to the plasma membrane. *Molecular Vision*. 2009;15(1):1806–18.
27. Tian G, Zhou Y, Hajkova D, Miyagi M, Dinculescu A, Hauswirth WW, et al. Clarin-1, encoded by the Usher Syndrome III causative gene, forms a membranous microdomain: possible role of clarin-1 in organizing the actin cytoskeleton. *J Biol Chem*. 2009;284(28):18980–93. <https://doi.org/10.1074/jbc.M109.003160> PMID: 19423712
28. Gopal SR, Chen DHC, Chou SW, Zang J, Neuhauss SCF, Stepanyan R, et al. Zebrafish models for the mechanosensory hair cell dysfunction in Usher syndrome 3 reveal that Clarin-1 is an essential hair bundle protein. *Journal of Neuroscience*. 2015;35(28):10188–201.
29. Geng R, Geller SF, Hayashi T, Ray CA, Reh TA, Bermingham-McDonogh O, et al. Usher syndrome IIIA gene clarin-1 is essential for hair cell function and associated neural activation. *Hum Mol Genet*. 2009;18(15):2748–60. <https://doi.org/10.1093/hmg/ddp210> PMID: 19414487
30. Geng R, Melki S, Chen D, Tian G, Furness D, Oshima-Takago T, et al. The mechanosensory structure of the hair cell requires clarin-1, a protein encoded by usher syndrome III causative gene. *Journal of Neuroscience*. 2012;32(28):9485–98.
31. Dulon D, Papal S, Patni P, Cortese M, Vincent P, Tertrais M. Clarin-1 gene transfer rescues auditory synaptopathy in model of Usher syndrome. *J Clin Invest*. 2018;128(8):3382–401.
32. Xu L, Bolch SN, Santiago CP, Dyka FM, Akil O, Lobanova ES, et al. Clarin-1 expression in adult mouse and human retina highlights a role of Müller glia in Usher syndrome. *J Pathol*. 2020;250(2):195–204. <https://doi.org/10.1002/path.5360> PMID: 31625146
33. Cowan CS, Renner M, De Gennaro M, Gross-Scherf B, Goldblum D, Hou Y. Cell types of the human retina and its organoids at single-cell resolution. *Cell*. 2020;182(6):1623–1640.e34. <https://doi.org/10.1016/j.cell.2020.08.021>
34. Lukowski SW, Lo CY, Sharov AA, Nguyen Q, Fang L, Hung SS, et al. A single-cell transcriptome atlas of the adult human retina. *EMBO J*. 2019;38(18):e100811. <https://doi.org/10.15252/embj.2018100811> PMID: 31436334
35. Hoang T, Wang J, Boyd P, Wang F, Santiago C, Jiang L, et al. Gene regulatory networks controlling vertebrate retinal regeneration. *Science*. 2020;370(6519):eabb8598. <https://doi.org/10.1126/science.abb8598> PMID: 33004674



36. Wilk M, Hickenpähler A, Collier R, Link B, Carroll J. The effect of retinal melanin on optical coherence tomography images. *Translational Vision Science & Technology*. 2017;6(2):8. <https://doi.org/10.1167/tvst.6.2.8>
37. Ernest S, Rauch GJ, Haffter P, Geisler R, Petit C, Nicolson T. Mariner is defective in myosin VIIA: a zebrafish model for human hereditary deafness. *Hum Mol Genet*. 2000;9(14):2189–96. <https://doi.org/10.1093/hmg/9.14.2189> PMID: 10958658
38. Nicolson T, Rüsch A, Friedrich R, Granato M, Ruppertsberg J, Nüsslein-Volhard C. Genetic analysis of vertebrate sensory hair cell mechanosensation: the zebrafish circler mutants. *Neuron*. 1998;20(2):271–83.
39. Seiler C, Finger-Baier KC, Rinner O, Makhankov YV, Schwarz H, Neuhauss SCF, et al. Duplicated genes with split functions: independent roles of protocadherin15 orthologues in zebrafish hearing and vision. *Development*. 2005;132(3):615–23. <https://doi.org/10.1242/dev.01591> PMID: 15634702
40. Cooper R, Wilk M, Tarima S, Carroll J. Evaluating descriptive metrics of the human cone mosaic. *Investigative Ophthalmology & Visual Science*. 2016;57(7):2992.
41. Crouzier L, Diez C, Richard EM, Cubedo N, Barbereau C, Rossel M, et al. Loss of Pde6a Induces Rod Outer Segment Shrinkage and Visual Alterations in pde6aQ70X Mutant Zebrafish, a Relevant Model of Retinal Dystrophy. *Front Cell Dev Biol*. 2021;9:675517. <https://doi.org/10.3389/fcell.2021.675517> PMID: 34095146
42. Meschede IP, Burgoyne T, Tolmachova T, Seabra MC, Futter CE. Chronically shortened rod outer segments accompany photoreceptor cell death in Choroideremia. *PLoS One*. 2020;15(11):e0242284. <https://doi.org/10.1371/journal.pone.0242284> PMID: 33201897
43. Cideciyan AV, Sudharsan R, Dufour VL, Massengill MT, Iwabe S, Swider M, et al. Mutation-independent rhodopsin gene therapy by knockdown and replacement with a single AAV vector. *Proc Natl Acad Sci U S A*. 2018;115(36):E8547–56. <https://doi.org/10.1073/pnas.1805055115> PMID: 30127005
44. Messchaert M, Dona M, Broekman S, Peters TA, Corral-Serrano JC, Slijkerman RWN, et al. Eyes shut homolog is important for the maintenance of photoreceptor morphology and visual function in zebrafish. *PLoS One*. 2018;13(7):e0200789. <https://doi.org/10.1371/journal.pone.0200789> PMID: 30052645
45. Nowakowski RS, Hayes NL. New neurons: extraordinary evidence or extraordinary conclusion?. *Science*. 2000;288(5467):771.
46. Cooper-Kuhn CM, Kuhn HG. Is it all DNA repair? Methodological considerations for detecting neurogenesis in the adult brain. *Brain Res Dev Brain Res*. 2002;134(1–2):13–21. [https://doi.org/10.1016/S0165-3806\(01\)00243-7](https://doi.org/10.1016/S0165-3806(01)00243-7) PMID: 11947933
47. Rakic P. Neurogenesis in adult primate neocortex: an evaluation of the evidence. *Nat Rev Neurosci*. 2002;3(1):65–71. <https://doi.org/10.1038/nrn700> PMID: 11823806
48. Copani A, Uberti D, Sortino MA, Bruno V, Nicoletti F, Memo M. Activation of cell-cycle-associated proteins in neuronal death: a mandatory or dispensable path?. *Trends Neurosci*. 2001;24(1):25–31. [https://doi.org/10.1016/S0166-2236\(00\)01663-5](https://doi.org/10.1016/S0166-2236(00)01663-5) PMID: 11163884
49. Becker EBE, Bonni A. Cell cycle regulation of neuronal apoptosis in development and disease. *Prog Neurobiol*. 2004;72(1):1–25. <https://doi.org/10.1016/j.pneurobio.2003.12.005> PMID: 15019174
50. Herrup K, Neve R, Ackerman SL, Copani A. Divide and die: cell cycle events as triggers of nerve cell death. *J Neurosci*. 2004;24(42):9232–9. <https://doi.org/10.1523/JNEUROSCI.3347-04.2004> PMID: 15496657
51. Zhang Z, Shan X, Li S, Chang J, Zhang Z, Dong Y, et al. Retinal light damage: From mechanisms to protective strategies. *Survey of Ophthalmology*. 2024;69(6):905–15.
52. Phillips JB, Kulis S, Buchner SH, Fox EJ, Wegner J, Peirce J, et al. Hexafluoro slows retinal degeneration and improves visual function in zebrafish models of Usher syndrome 1F. 2023. <https://doi.org/10.1101/2023.12.29.573664>
53. Riedl J, Crevenna AH, Kessenbrock K, Yu JH, Neukirchen D, Bista M, et al. Lifeact: a versatile marker to visualize F-actin. *Nat Methods*. 2008;5(7):605–7. <https://doi.org/10.1038/nmeth.1220> PMID: 18536722
54. Donnelly M, Luke G, Mehrotra A, Li X, Hughes L, Gani D. Analysis of the aphthovirus 2A/2B polyprotein “cleavage” mechanism indicates not a proteolytic reaction, but a novel translational effect: a putative ribosomal “skip.” *J Gen Virol*. 2001;82(5):1013–25.
55. Vihtelic TS, Hyde DR. Light-induced rod and cone cell death and regeneration in the adult albino zebrafish (*Danio rerio*) retina. *Journal of Neurobiology*. 2000;44(3):289–307.
56. Thomas JL, Nelson CM, Luo X, Hyde DR, Thummel R. Characterization of multiple light damage paradigms reveals regional differences in photoreceptor loss. *Exp Eye Res*. 2012;97(1):105–16. <https://doi.org/10.1016/j.exer.2012.02.004> PMID: 22425727

57. Vaughan DK, Coulibaly SF, Darrow RM, Organisciak DT. A morphometric study of light-induced damage in transgenic rat models of retinitis pigmentosa. *Invest Ophthalmol Vis Sci*. 2003;44(2):848–55. <https://doi.org/10.1167/iov.02-0709> PMID: [12556421](#)
58. Grimm C, Wenzel A, Hafezi F, Yu S, Redmond TM, Remé CE. Protection of Rpe65-deficient mice identifies rhodopsin as a mediator of light-induced retinal degeneration. *Nat Genet*. 2000;25(1):63–6. <https://doi.org/10.1038/75614> PMID: [10802658](#)
59. Li Y, Cohen ED, Qian H. Rod and Cone Coupling Modulates Photopic ERG Responses in the Mouse Retina. *Front Cell Neurosci*. 2020;14:566712. <https://doi.org/10.3389/fncel.2020.566712> PMID: [33100974](#)
60. Zelinger L, Wissinger B, Eli D, Kohl S, Sharon D, Banin E. Cone dystrophy with supernormal rod response: novel KCNV2 mutations in an underdiagnosed phenotype. *Ophthalmology*. 2013;120(11):2338–43. <https://doi.org/10.1016/j.ophtha.2013.03.031> PMID: [23725738](#)
61. Esteves-Leandro J, Torres-Costa S, Estrela-Silva S, Santos-Silva R, Brandão E, Grangeia A. Cone dystrophy with supernormal rod responses: A rare KCNV2 gene variant. *European Journal of Ophthalmology*. 2022;32(1):664–72.
62. Ogun O, Zallocchi M. Clarin-1 acts as a modulator of mechanotransduction activity and presynaptic ribbon assembly. *J Cell Biol*. 2014;207(3):375–91. <https://doi.org/10.1083/jcb.201404016> PMID: [25365995](#)
63. Kwan KM, Fujimoto E, Grabher C, Mangum BD, Hardy ME, Campbell DS, et al. The Tol2kit: a multisite gateway-based construction kit for Tol2 transposon transgenesis constructs. *Dev Dyn*. 2007;236(11):3088–99. <https://doi.org/10.1002/dvdy.21343> PMID: [17937395](#)
64. Hall TE, Martel N, Ariotti N, Xiong Z, Lo HP, Ferguson C. In vivo cell biological screening identifies an endocytic capture mechanism for T-tubule formation. *Nature Communications*. 2020;11:3711. <https://doi.org/10.1038/s41467-020-17573-5>
65. Flatter J, Cooper R, Dubow M, Pinhas A, Singh R, Kapur R. Outer retinal structure following closed globe blunt ocular trauma. *Retina*. 2014;34(10):2133–46.
66. Gao P, Qin Y, Qu Z, Huang Y, Liu X, Li J, et al. The Zpr-3 antibody recognizes the 320-345 region of Rho and labels rods and green cones in zebrafish. *bioRxiv*. 2022. <https://doi.org/10.1101/2022.02.21.481375v1>
67. Scoles D, Flatter JA, Cooper RF, Langlo CS, Robison S, Neitz M, et al. Assessing photoreceptor structure associated with ellipsoid zone disruptions visualized with optical coherence tomography. *Retina*. 2016;36(1):91–103. <https://doi.org/10.1097/IAE.0000000000000618> PMID: [26166796](#)
68. Brastrom LK, Scott CA, Dawson DV, Slusarski DC. A High-Throughput Assay for Congenital and Age-Related Eye Diseases in Zebrafish. *Biomedicine*. 2019;7(2):28. <https://doi.org/10.3390/biomedicine7020028> PMID: [30979021](#)
69. Vinberg F, Kolesnikov AV, Kefalov VJ. Ex vivo ERG analysis of photoreceptors using an in vivo ERG system. *Vision Res*. 2014;101:108–17. <https://doi.org/10.1016/j.visres.2014.06.003> PMID: [24959652](#)